Slow Light Cavities for Thermal Noise Mitigation in Laser Frequency Stabilization

Lindén, Marcus

2025

Document Version:
Publisher's PDF, also known as Version of record

Link to publication

Citation for published version (APA):
Lindén, M. (2025). *Slow Light Cavities for Thermal Noise Mitigation in Laser Frequency Stabilization*. Department of Physics, Lund University.

Total number of authors:
1

Creative Commons License:
CC BY

General rights
Unless other specific re-use rights are stated the following general rights apply:
Copyright and moral rights for the publications made accessible in the public portal are retained by the authors and/or other copyright owners and it is a condition of accessing publications that users recognise and abide by the legal requirements associated with these rights.

- Users may download and print one copy of any publication from the public portal for the purpose of private study or research.
- You may not further distribute the material or use it for any profit-making activity or commercial gain
- You may freely distribute the URL identifying the publication in the public portal

Read more about Creative commons licenses: https://creativecommons.org/licenses/

Take down policy
If you believe that this document breaches copyright please contact us providing details, and we will remove access to the work immediately and investigate your claim.

LUND UNIVERSITY

PO Box 117
221 00 Lund
+46 46-222 00 00

Download date: 11. Jun. 2026

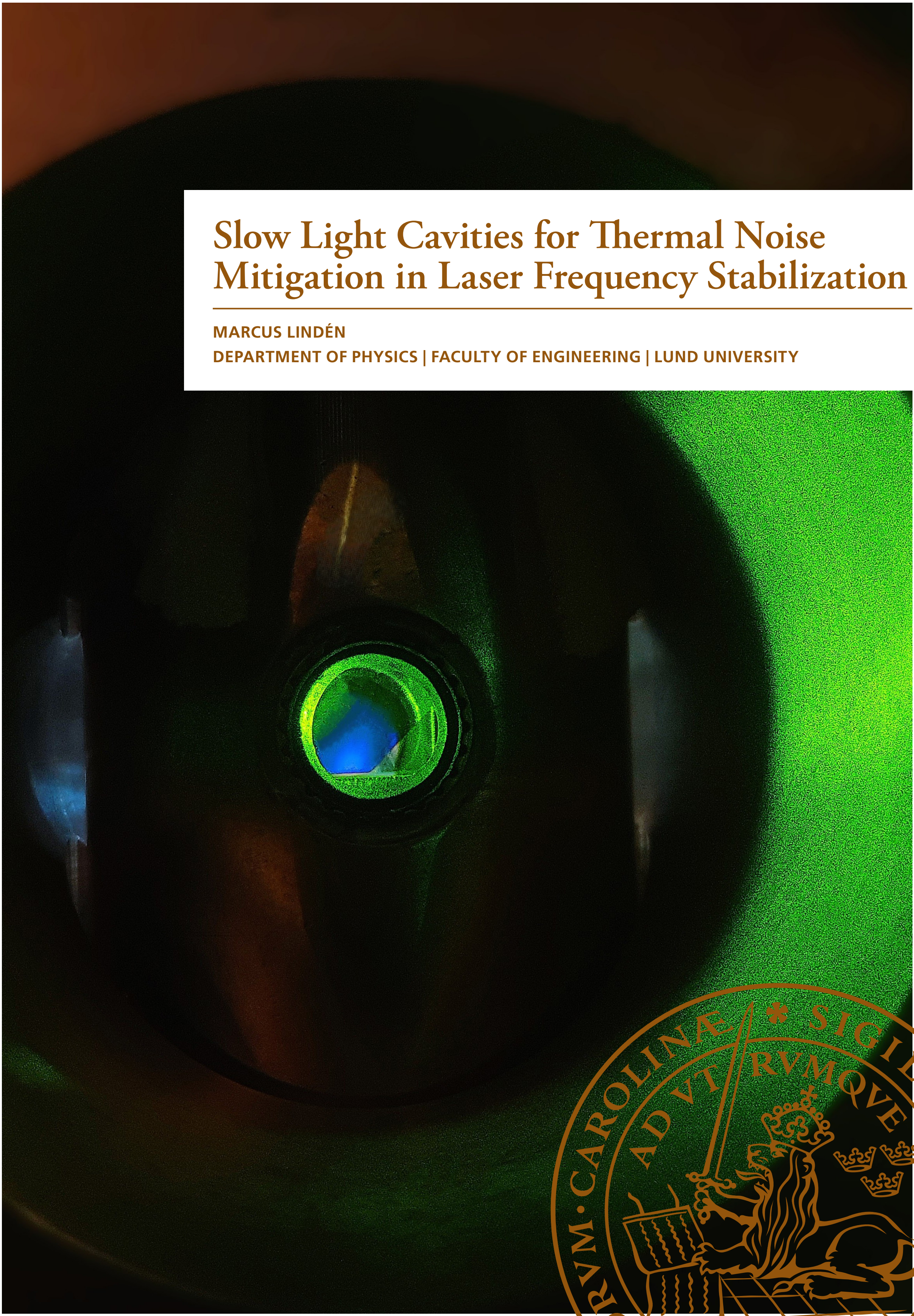

Slow Light Cavities for Thermal Noise Mitigation in Laser Frequency Stabilization

MARCUS LINDÉN

DEPARTMENT OF PHYSICS | FACULTY OF ENGINEERING | LUND UNIVERSITY

Slow Light Cavities for Thermal Noise Mitigation in Laser Frequency Stabilization

Slow Light Cavities for Thermal Noise Mitigation in Laser Frequency Stabilization

by Marcus Lindén

Thesis for the degree of Doctor of Philosophy
Thesis advisors: Dr. Lars Rippe, Prof. Stefan Kröll, Dr. Martin Zelan
Faculty opponent: Dr. habil. Yann Le Coq

To be presented, with the permission of the Faculty of Engineering of Lund University, for public criticism in the Rydberg lecture hall on Friday, the 13th of June 2025 at 09:15.

DOKUMENTDATABLAD enl SIS 61 41 21

Organization
LUND UNIVERSITY

Department of Physics
Box 118
SE–221 00 LUND
Sweden

Document name
DOCTORAL DISSERTATION

Date of disputation
2025-06-13

Sponsoring organization
RISE Research Institutes of Sweden AB

Author(s)
Marcus Lindén

Title and subtitle
Slow Light Cavities for Thermal Noise Mitigation in Laser Frequency Stabilization

Abstract

Precision laser frequency stabilization is an important part of modern optical metrology, with applications ranging from atomic clocks to fundamental tests of physics. However, the frequency stability of the ultrastable cavities used in these experiments is fundamentally limited by thermal noise in the mirrors of the cavity. The thermal noise causes the atoms that form the mirrors to move randomly, which results in small variations in the length of the cavity used as a reference.

This thesis explores a design based on slow-light cavities, which are optical resonators characterized by strong dispersion. The dispersion effectively increases the optical path length of the cavity, resulting in reduced sensitivity to cavity length changes due to thermal fluctuations. The cavity was constructed from a yttrium orthosilicate crystal doped with the rare-earth element europium, coated with plane-parallel mirrors. These ions have narrow optical transitions and long hyperfine lifetimes, so that highly dispersive transmission windows can be created in the inhomogeneous profile via optical pumping. The frequency stability was assessed in the presence of such strong dispersion where the group velocity of light is drastically reduced. A dual beam interrogation scheme is then introduced to measure the differential short-term frequency stability of the locked laser system. The results show that careful alignment of the cavity modes within the transmission window can significantly mitigate drift, which is important to improve frequency stability by enabling longer averaging times.

A method to reset the population in longlived hyperfine states of rare-earth ions to thermal equilibrium is also demonstrated. This method was used to restore the locking conditions of the transmission window after it had been degraded by the locking beam, enabling subsequent locking at the same frequency.

Key words
slow light effect, laser frequency stabilization, optical clocks, rare earths

Classification system and/or index terms (if any)

Supplementary bibliographical information

Language
English

ISSN and key title
0281-2762, LRAP-611

ISBN
978-91-8104-533-8 (print)
978-91-8104-534-5 (pdf)

Recipient's notes

Number of pages
159

Price

Security classification

I, the undersigned, being the copyright owner of the abstract of the above-mentioned dissertation, hereby grant to all reference sources the permission to publish and disseminate the abstract of the above-mentioned dissertation.

Signature ______________________ Date 2025-04-14

Slow Light Cavities for Thermal Noise Mitigation in Laser Frequency Stabilization

by Marcus Lindén

LUND
UNIVERSITY

A doctoral thesis at a university in Sweden takes either the form of a single, cohesive research study (monograph) or a summary of research papers (compilation thesis), which the licentiate student has written alone or together with one or several other author(s).

In the latter case the thesis consists of two parts. An introductory text puts the research work into context and summarizes the main points of the papers. Then, the research publications themselves are reproduced, together with a description of the individual contributions of the authors. The research papers may either have been already published or are manuscripts at various stages (in press, submitted, or in draft).

Cover: View of the Eu:YSO slow light cavity through the cryostat window

Funding information: This thesis work was partially supported by the Knut and Alice Wallenberg Foundation through the Wallenberg Centre for Quantum Technology (WACQT), EMPIR (European Metrology Programme for Innovation and Research), and the Swedish Research Council.

Pages 1–83 © 2025 Marcus Lindén
Paper I © 2025 The authors
Paper II © 2025 The authors
Paper III © 2024 Optica Publishing Group (Open Access Publishing Agreement)
Paper IV © 2024 The authors
Paper V © 2025 The authors

Faculty of Engineering, Department of Physics

ISBN: 978-91-8104-533-8 (print)
ISBN: 978-91-8104-534-5 (pdf)
ISSN: 0281-2762, LRAP-611

Printed in Sweden by Media-Tryck, Lund University, Lund 2025

NORDIC SWAN ECOLABEL
Printed matter
3041 0903

Media-Tryck is a Nordic Swan Ecolabel certified provider of printed material. Read more about our environmental work at www.mediatryck.lu.se

MADE IN SWEDEN

Till morfar.

Contents

Abstract

Precision laser frequency stabilization is an important part of modern optical metrology, with applications ranging from atomic clocks to fundamental tests of physics. However, the frequency stability of the ultrastable cavities used in these experiments is fundamentally limited by thermal noise in the mirrors of the cavity. The thermal noise causes the atoms that form the mirrors to move randomly, which results in small variations in the length of the cavity used as a reference.

This thesis explores a design based on slow-light cavities, which are optical resonators characterized by strong dispersion. The dispersion effectively increases the optical path length of the cavity, resulting in reduced sensitivity to cavity length changes due to thermal fluctuations. The cavity was constructed from a yttrium orthosilicate crystal doped with the rare-earth element europium, coated with plane-parallel mirrors. These ions have narrow optical transitions and long hyperfine lifetimes, so that highly dispersive transmission windows can be created in the inhomogeneous profile via optical pumping. The frequency stability was assessed in the presence of such strong dispersion where the group velocity of light is drastically reduced. A dual beam interrogation scheme is then introduced to measure the differential short-term frequency stability of the locked laser system. The results show that careful alignment of the cavity modes within the transmission window can significantly mitigate drift, which is important to improve frequency stability by enabling longer averaging times.

A method to reset the population in longlived hyperfine states of rare-earth ions to thermal equilibrium is also demonstrated. This method was used to restore the locking conditions of the transmission window after it had been degraded by the locking beam, enabling subsequent locking at the same frequency.

List of publications

This thesis is based on the following publications, referred to by their Roman numerals:

I **Highly tuneable cryogenic radio-frequency magnetic field transmitter coil using resonant in-situ switch bank tuning**
M. Lindén, D. Gustavsson, K. Shortiss, L. Rippe
Manuscript in preparation, estimated submission: May, 2025

II **Resetting long-lived ground states in Eu:YSO using a highly tunable radio-frequency transmitter coil circuit**
M. Lindén, D. Gustavsson, A. Walther, A. Kinos, L. Rippe
Manuscript in preparation, estimated submission: May, 2025

III **Using slow light to enable laser frequency stabilization to a short, high-Q cavity**
D. Gustavsson, **M. Lindén**, K. Shortiss, S. Kröll, A. Walther, A. Kinos, L. Rippe
Opt. Express 33, 2025, 2866-2877

IV **Pushing the limits of negative group velocity**

A. J. Renders, D. Gustavsson, **M. Lindén**, A. Walther, S. Kröll, A. Kinos, L. Rippe
arXiv, 2024, 2404.04771

V **Characterization of intrinsic Brownian noise in slow light cavities via dual-beam interrogation**
M. Lindén, A. J. Renders, D. Gustavsson, A. Kinos, A. Walther, S. Kröll, M. Zelan, L. Rippe
Manuscript in preparation, estimated submission: June, 2025

All papers are reproduced with permission of their respective publishers.

Acknowledgements

I would like to begin by thanking my main supervisor, Lars Rippe, for always lending a helping hand with enthusiasm, having patience with my questions, and showing support throughout. It meant a lot to me. Then I would also like to thank my co-supervisor Stefan Kröll for his wise advice and guidance in discussions and for making my time in the group so positive. My third co-supervisor, Martin Zelan, for his constructive insights, inspiration, and talks about skiing and life in general. I thank Adam Kinos for all the help with simulations and for being a good teacher, and Andreas Walther for his explanation of physics and interesting ideas.

To the other group members, especially David, Kevin, and Johan for all the good times in the lab. Hafsa, Alexander, Jiayu, Erik, Mohammed, Egle, Akvile, David (H), Abdullah, and Maria for the lunches, coffee breaks, group activities, and for making it a joy to be at work. I would also like to give an extra thanks to Jörgen at RISE for being a great manager and including me in activities although I was located far from the work site, Åke for helping me with anything related to computers and electronics, Maria for the support regarding financial issues, and of course the rest of the division members for all the good times and positive, welcoming spirit.

I have had a great time in Lund and for that I owe partly to my fellow floor ball crew, people over at NanoLund, and people I met along the way. You made my stay here memorable.

Lastly, I have to thank my family. While I did not get to see you that often, you never felt far away.

Populärvetenskaplig sammanfattning

Tid är något vi alla upplever. Vi ser sekunderna ticka förbi på en klocka, betraktar solen gå upp och ned och känner dagarna passera. Men om vi försöker förklara vad tid egentligen är, blir det snabbt svårt att sätta ord på det. Utspelar sig tiden ögonblick för ögonblick, där framtiden är öppen och osäker? Eller är allt redan bestämt, likt en bok där dåtid, nutid och framtid är fixerade och vi bara upptäcker varje ögonblick när vi rör oss genom dem?

Tiden har utvecklats under miljarder år—galaxer bildades, stjärnor slocknade och universum utvecklades långt innan människan kom. Tiden tycks vara invävd i själva strukturen av universum och ger denna en existentiell ram. Sättet vi mäter tid på, med klockor och kalendrar, är dock en mänsklig uppfinning för att förstå förändringar och organisera händelser.

I vårt vardagsliv antar vi ofta att klockors tickande sker i jämn takt, men fysiken berättar ibland en annan historia. Under särskilda omständigheter kan tiden sakta in. Det är inte bara ett abstrakt resonemang utan en verklig och mätbar effekt. När gravitationen är mycket stark, eller när objekt rör sig med hög hastighet kan själva tiden sträckas ut, eller dras ihop, något som strider mot vår vardagliga intuition.

Genom att använda extremt exakta klockor, som delar in tiden i mycket små intervaller, kan vi visa att tiden faktiskt går olika fort på olika höjder och vid olika hastigheter. Astronauter ombord på den internationella rymdstationen upplever tiden något långsammare än människor på jordens yta. När de till slut återvänder har de därför åldrats en aning mindre än vi andra.

Det finns mycket vi ännu inte vet om tidens natur. Genom att förbättra våra metoder för att mäta tid kanske vi kan avslöja några av dess mysterier. För detta krävs dock ytterst noggranna klockor. De mest precisa klockor som människan har byggt styrs inte av kugghjul utan av ljus. Dessa klockor innehåller en oscillator som svänger med en jämn rytm, ungefär som ett pendelur, men här är det ljusets elektriska fält som svänger med mycket hög och exakt frekvens. Denna frekvens bestäms av en optisk kavitet, ett litet utrymme där ljuset från en laser reflekteras fram och tillbaka mellan två speglar. Bara vissa frekvenser passar i kaviteten, de där ljusvågorna studsar mellan speglarna på ett sätt som tillåter att de förstärker varandra.

Om avståndet mellan speglarna kunde hållas helt konstant skulle detta ge upphov till extremt regelbundna tick, vilket i princip kan användas för att mäta tid med mycket hög noggrannhet. Men i praktiken är detta mycket svårt. Även de mest stabila oscillatorerna påverkas av ytterst små rörelser i speglarna, orsakade av att atomer ständigt vibrerar. Det gör att kavitetens längd förändras en aning, vilket får frekvensen att svaja. Det är som om pendeln i ett ur hela tiden ändrade sin längd. Dessa små, slumpmässiga variationer leder till att klockan tickar en aning oregelbundet, vilket skapar brus i rytmen.

I denna avhandling undersöks möjligheten att använda ljus som bromsats ned till hastigheten av ett flygplan. Den kraftiga sänkningen av ljusets hastighet är möjlig tack vare specialmaterial bestående av sällsynta jordartsmetaller. När ljuset rör sig långsammare minskar känsligheten för små förändringar i kavitetens längd. Det beror på att ljuset ”upplever” kaviteten som mycket längre än den faktiskt är. Därmed påverkar små variationer i längden frekvensen betydligt mindre än i en vanlig kavitet. Resultatet blir att frekvensen, och därmed tickandet, kan göras avsevärt mer stabilt.

I slutändan hoppas vi kunna bygga en klocka så exakt att den kan användas för nya teknologiska tillämpningar, såsom förbättrade GPS-system, känsligare gravitationsdetektorer och en djupare förståelse av tidens natur. Genom att fortsätta utveckla klockor kan vi inte bara mäta tid bättre, utan också få nya insikter om universum självt.

Slow Light Cavities for Thermal Noise Mitigation in Laser Frequency Stabilization

Chapter 1

Introduction

1.1 Measuring time

Long before the invention of clocks, humans experienced time through the rhythms of nature: the rise and setting of the sun, the phases of the moon, and the changing seasons. These natural cycles governed hunting, farming, migration, and social rituals. Although early societies did not have tools to precisely measure time, their survival depended on recognizing patterns and anticipating changes. The need to track time more deliberately grew with the complexity of human life. Agricultural societies needed to plan harvests, religious groups observed rituals at specific times, and trade required coordination across distances. These pressures gradually turned a passive observation of time into an active desire to measure it.

One of the earliest structured methods of timekeeping was the water clock, known as a *clepsydra*[1] (see Fig. 1.1). The water would drip steadily from a small hole at the bottom of a vessel into a marked container. As the container filled, the rising water level could be used to approximate the passage of time. The key to the effectiveness of the clepsydra was the steady, unchanging rate at which the water dripped. Any fluctuation in flow would make the markings meaningless, causing the time to be measured inconsistently.

This method of tracking time illustrates an important concept in modern timekeeping. The dripping water container acts as a simple form of *oscillator*, producing a steady and regular series of drops. The marked container keeps track of how many of these reference events have occurred, acting

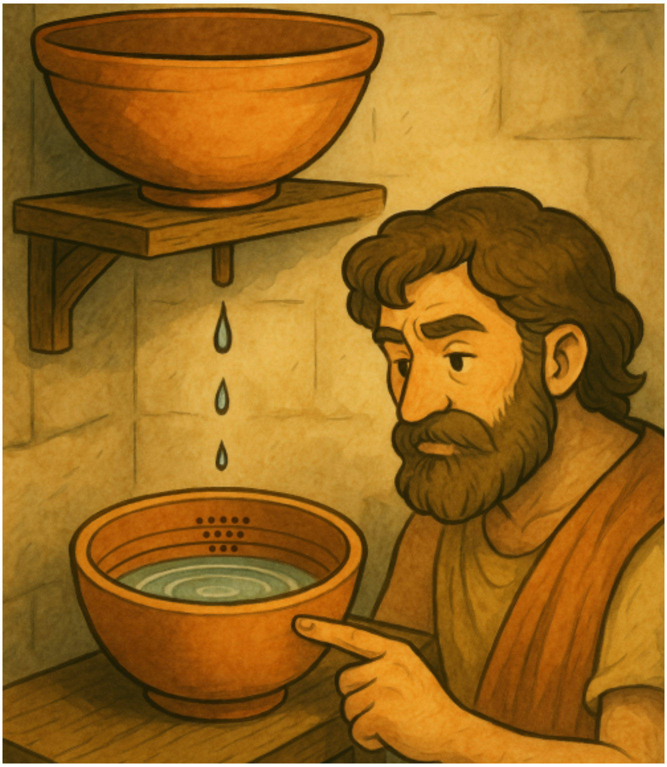

Figure 1.1: Ancient timekeeping. The clepsydra, meaning "water thief" in Greek, was one of the earliest timekeeping devices. The steady flow of water served as a means to track the passage of time.

as a *counter*. To relate the markings to a meaningful time, they can be calibrated against a known *frequency reference*, such as the rotation of the Earth. Together, they form a *clock*: a system that counts and organizes these oscillations to define meaningful time intervals to track the passage of time throughout the day. Without a stable and predictable oscillator, a clock cannot reliably measure time, just as inconsistent water flow would have rendered early water clocks inaccurate.

1.2 From water clocks to maritime navigation

Early civilizations used water clocks and sundials to track time, but these methods were imprecise and dependent on environmental conditions. The mechanical clock, developed in the 14th century, revolutionized timekeeping by providing a self-contained system independent of the sun or flowing water. By the 17th century, Galileo Galilei and Christiaan Huygens refined the pendulum clock, bringing timekeeping precision to within seconds per day.

As timekeeping technology advanced, so did its applications. In the 17th century, accurate timekeeping became especially important for maritime navigation. Although pendulum clocks, refined by Galileo and Huygens, had brought significant improvements in timekeeping precision on land, they were impractical at sea due to the constant motion of ships. Navigators instead relied heavily on mechanical clocks, sextants, and observations of celestial bodies to determine their position. However, even small inaccuracies in their clocks could lead ships disastrously astray. An error of just a few minutes could send a vessel hundreds of kilometers off course, turning routine voyages into dangerous journeys into uncharted waters.

This danger was tragically demonstrated in 1707 when Admiral Sir Cloudesley Shovell's fleet, miscalculating its location due to inaccurate timekeeping, struck rocks off the Isles of Scilly. More than 1,400 sailors lost their lives in one of Britain's worst maritime disasters. This catastrophe, among others, prompted the British Parliament to announce the Longitude Prize in 1714, seeking a reliable method of determining longitude at sea.[2]

John Harrison, a self-taught clockmaker, dedicated the rest of his life to solving this problem. He designed and refined marine chronometers capable of keeping precise time despite challenging maritime conditions. Harrison's marine chronometers greatly improved navigation, reducing longitude errors from hundreds of kilometers to about 20–50 kilometers.

1.3 Modern era timekeeping

While the Harrison's chronometers represented a highlight of mechanical timekeeping, the next major advances came with the development of electronic techniques. In the 20th century, clocks using piezoelectric quartz crystal oscillators could achieve precision on the order of milliseconds per day. However, the greatest breakthrough in the modern era came with atomic clocks which rely on the precise frequency of atomic transitions to define time itself. The second, officially defined by the International System of Units (SI), is based on 9,192,631,770 cycles of electromagnetic radiation that corresponds to the transition between two hyperfine energy levels of the ground state of cesium-133 atoms.[3,4] While atomic clocks based on microwave transitions in cesium have been the standard for timekeeping for decades, the next revolution in precision lies in optical clocks. These clocks use transitions in atoms or ions that oscillate at much higher frequencies (hundreds of trillions of times per second) compared to the microwave transitions of cesium.

The best optical oscillators today are lasers stabilized to ultrastable Fabry-Pérot (FP) cavities, which act as a stable physical reference to provide highly regular oscillations, the so-called ticks of the clock. These oscillators are approaching short-term frequency stability on the order of 10^{-17} [5]. By also locking the oscillator to an extremely narrow atomic transition, long-term stability can reach 10^{-18} [6,7]. Using lasers locked to ultrastable cavities (oscillator), laser-cooled atomic systems (frequency references), and optical frequency combs (counters), optical clocks have surpassed microwave-based atomic clocks in accuracy. In fact, the systematic uncertainty evaluated that quantifies the accuracy of the clock has become so low that optical clocks are currently being explored for the redefinition of the SI second.[8]

Better oscillators are important for atomic clocks because they enable longer and more coherent interrogation of the atomic transition, which in turn allows for higher resolution and faster averaging of frequency measurements. If the oscillator is not sufficiently stable, its frequency noise during interrogation degrades the ability to resolve the transition precisely, ultimately limiting the precision of the clock and practical performance. What currently limits the stability in state-of-the-art FP cavities is variations in the cavity length due to the very small movement of atoms forming the mirrors, caused by thermal noise. Because the laser is locked to this cavity, these length fluctuations will translate directly into the frequency noise of the laser. This effect can typically be reduced by making the cavity longer as the fractional length change is reduced. However, there is a limit to how long a cavity can be before mechanical noise becomes significant. In practice, the longest cavities built today are about 50 cm.

This thesis explores the use of slow light cavities as a stable reference for lasers. In slow light cavities, interference effects lead to a reduction in group velocity, causing light to experience a longer delay as it travels through the medium. Although the physical path length does not change, the increased delay can be interpreted as light effectively propagating over a longer distance. The effective length of the cavity can be longer than 10 km in highly dispersive materials, providing an alternative path to improve the optical frequency stability of cavities.

1.3.1 Outline of thesis

This thesis explores the use of slow light cavities to enhance laser frequency stabilization by effectively increasing the effective length of the cavity, thereby reducing the sensitivity to thermal noise. The second chapter provides an overview of laser frequency stabilization using the Pound–Drever–Hall (PDH) technique, including its principles, practical implementation, and limitations.

Chapter 3 discusses rare-earth-ion-doped materials. It focuses on Eu:YSO due to the long-lived spectral holes and narrow homogeneous linewidths available in this material. Such optical properties enable the creation of highly dispersive cavities via spectral tailoring.

Chapter 4 addresses the challenge of resetting long-lived states in rare-earth ion-doped materials to equilibrium. Slow light laser stabilization requires some form of reset mechanism to perform sequential locking at the same frequency. This chapter explains how radio frequency magnetic fields resonant with the hyperfine transitions can be used to do so.

In Chapter 5, the thesis details the cavity performance under high dispersion and how locking is performed in this regime. Short-term stability measurements are presented for this type of cavity. A dual beam interrogation method is also introduced, which is used to characterize the differential short-term stability of the cavity.

The final chapter concludes this thesis and outlines future directions and experiments for slow light frequency stabilization.

Chapter 2

Frequency stabilization of lasers

Optical precision timekeeping is based on the ability to stabilize the frequency of a laser to an extreme degree of accuracy, where the laser constitutes the frequency generating element in the clock. Lasers that have been tied to some stable physical reference to increase the short-stability of atomic clocks have played a significant role in advancing fundamental physics and precision metrology. Such lasers enable measurements of time variation in fundamental constants[9], tests of relativity[10], gravitational wave detection[11,12], and dark matter searches[7,13]. As even the smallest frequency fluctuations can introduce significant measurement errors, it is important that these lasers have high short-term stability. To achieve such a level of stability, lasers must maintain coherence over the relevant time scale, necessitating techniques to suppress frequency noise. A widely adopted approach is the use of ultrastable Fabry-Pérot cavities to provide a high-finesse optical reference. By locking a laser to a cavity, its coherence length can be extended and its short-term frequency stability improved. These lasers enable measurements of time variation in fundamental constants[9], tests of relativity[10], gravitational wave detection[11,12], and dark matter searches[7,13].

The Fabry-Pérot cavity is an optical resonator formed by two, typically highly reflective mirrors, separated by a fixed distance. Light entering the cavity undergoes multiple reflections, leading to constructive and destructive interference, which governs the cavity's transmission properties. The resonance frequencies of the cavity are determined by the condition that an integer number of half-wavelengths fit precisely within the cavity length. This results in discrete resonances spaced by the free spectral range (FSR), given by:

$$\nu_{\mathrm{FSR}} = \frac{c}{2L}, \tag{2.1}$$

where c is the speed of light and L the cavity length. The linewidth of a resonance mode, $\Delta\nu$, is related to the finesse of the cavity $\mathcal{F}$ and ν_{FSR} as:

$$\Delta\nu_{\mathrm{cav}} = \frac{\nu_{\mathrm{FSR}}}{\mathcal{F}} = \frac{c}{2L\mathcal{F}} \tag{2.2}$$

A longer cavity length and high finesse thus result in narrowing of the linewidth.

2.1 Pound-Drever-Hall locking

To exploit the stability of a Fabry-Pérot cavity for laser frequency stabilization, the laser must be actively locked to a cavity mode. In this context, locking means maintaining the laser frequency at the resonance frequency of the cavity, so that the laser inherits the frequency stability of the cavity. The cavity acts as a stable reference, transferring its mechanical stability to the optical domain. The locking process is typically implemented using the Pound-Drever-Hall (PDH) technique, which was proposed by Drever et al. in 1983.[14,15]

The method works by detecting how the frequency of a laser deviates from a cavity resonance and feeding that information back to correct the laser. This is achieved by phase modulating the laser to create sidebands around the carrier frequency and sending the light onto the cavity. When the laser is exactly on resonance, the carrier couples into the cavity and is transmitted, while the sidebands, being far off resonance, are reflected. However, when the laser is slightly detuned, the interference between the reflected light from the cavity and sidebands creates a beat signal whose phase depends on the direction of the detuning. By demodulating the reflected light at the modulation frequency, an asymmetric error signal is produced that crosses zero at resonance and changes sign depending on the frequency offset. This signal is then used in a feedback loop to stabilize the laser frequency to the cavity resonance. Thus, using the PDH technique we can effectively *lock* the laser to the cavity mode, suppressing frequency noise and enabling the laser to inherit the frequency stability of the cavity. In Ch. 5 we will take a closer look at how this is done in the case of our slow light cavity. This thesis explores the use of two independent locking loops simultaneously, but the principle for locking each loop is the same.

2.2 Limitations

Despite the effectiveness of PDH locking to suppress frequency noise, fundamental noise sources impose ultimate limits on the stability of a laser locked to a Fabry-Pérot cavity. The most significant contribution arises from thermomechanical noise, which is a result of Brownian motion of atoms within the cavity spacer and mirror coatings.[16,17] The movement of the atoms leads to very small length fluctuations in the cavity, which directly impact the resonance frequency of the cavity mode. The relationship governing the frequency stability for a cavity is:

$$\frac{\mathrm{d}\nu}{\nu} = -\frac{\mathrm{d}L}{L}. \tag{2.3}$$

where ν is the laser frequency and L the length of the cavity. This relation illustrates that any fluctuations in the cavity length ($\mathrm{d}L$) translate directly into frequency fluctuations of the stabilized laser ($\mathrm{d}\nu$). These fluctuations are not corrected by the PDH locking loop, as they arise from changes in the resonance frequency of the reference cavity itself. Therefore, to achieve high stability, the cavity must be able to effectively mitigate thermal noise.

This noise source is strongly dependent on the material properties, as indicated by the Fluctuation Dissipation Theorem.[18] A typical approach to reduce Brownian noise is to use materials with low mechanical loss for the cavity, including spacer, substrate, and mirror coatings.[19] However, the dominant source of thermal noise arises from mirror coatings.[20] Conventional cavities typically use mirror coatings made out of a dielectric stack of amorphous materials ($\mathrm{SiO_2/Ta_2O_5}$). Although efforts have been made to improve these coatings, they are still limited by mechanical dissipation due to internal friction (mechanical dampening).[21,22] In contrast, the growth of monocrystalline layers increases the stiffness of the material, thus constraining the atomic motion and reducing the mechanical dissipation. These coatings, typically made of AlGaAs/GaAs, have shown an order of magnitude improvement in mechanical loss.[23,24]

The noise can also be mitigated by lowering the temperature. As the noise scales as $\sqrt{T}$ where T is the absolute temperature of the atoms, there is gain in keeping these cavities at cryogenic temperatures.[25] Thus, going from room temperature to the temperature of our cryostat ($\sim 2\,\mathrm{K}$) yields a magnitude improvement in thermal noise. Further reduction of temperature (for example, in the mK range) can present a more technical challenge while also imposing stricter size restrictions on the experimental setup.

Other strategies involve increasing the length of the cavity or increasing the size of the optical mode in the mirrors[18]. Using a larger beam radius means that more atoms are probed across the mirror face, which averages the noise down. It scales as the square root of the area and is linearly proportional to the radius of the beam.[16]

The fractional frequency noise decreases as the cavity length increases, following a dependency of $1/\sqrt{L}$ for the spacer contribution and $1/L$ for the substrate and coating contributions.[17] The effect here is that the relative length changes $\mathrm{d}L/L$ become smaller for longer cavities. Increasing the cavity length past 50 cm is difficult, as the mechanical stability of the cavity is reduced.

In this thesis, we focus on increasing the optical length of the cavity. Although this is done at cryogenic temperatures, we can achieve better noise scaling by increasing the optical length of the cavity compared to cooling, as this scales linearly (Eq. 2.3). In Ch. 5 we shall see how slow light can help us in this regard by extending the cavity length by many orders of magnitude beyond the state-of-the-art cavities used today.

Chapter 3

Rare earth materials for quantum applications

Rare earth elements (RE), comprising the fifteen lanthanides from lanthanum (La) to lutetium (Lu), along with scandium (Sc) and yttrium (Y), form a chemically similar group of elements that play a fundamental role in modern materials science, photonics, and quantum technology. Despite their name, most rare-earth elements are relatively abundant in the Earth's crust, though their extraction and purification are often complex due to their geochemical similarities.[26]

The discovery of RE elements has an interesting history rooted in the late 18th century. In 1787, Swedish Army Lieutenant Carl Axel Arrhenius discovered an unusually heavy black mineral in a quarry near the village of Ytterby, Sweden. This mineral, later named gadolinite, became the source from which several RE elements were first identified, including yttrium (Y), erbium (Er), terbium (Tb), and ytterbium (Yb).[27] Notably, the small village of Ytterby has the distinction of having more elements named after it than any other location.

3.1 Host materials

Rather than being studied as isolated (free) ions, rare-earth elements are typically embedded in a crystal host lattice such as yttrium orthosilicate (YSO), lithium niobate (LN) or aluminum garnet from yttrium (YAG).

Embedding ions into solids offers important advantages. Free ions are highly reactive and difficult to confine in a stable, controlled environment over extended timescales. In addition, rare-earth ions in free space experience Doppler broadening due to their thermal motion, which obscures the fine structure of their energy levels.[28,29] In contrast, doping into host crystals like YSO allows the ions to remain in a well-defined, low-symmetry crystal field environment. This stabilizes them spatially and enables precise control and measurement of the energy level structure. Because the inner electrons of the rare earth ions are shielded from the surrounding crystal, their optical properties remain similar to those of the free ions, even in a solid. Since dopant concentrations are typically low (below 1 %), bulk properties such as refractive index, thermal characteristics, and hardness of the crystal are largely unchanged.

High-quality single crystals used for rare-earth doping are commonly grown using the Czochralski method. In this method, a small seed crystal is dipped into a molten material and slowly pulled upward while rotating, allowing atoms to arrange themselves into an ordered lattice around the seed.[30] Doping a crystal typically involves adding a small amount of the dopant to the melt during crystal growth. As the crystal (or boule) forms, some of the host ions in the lattice are naturally substituted by dopant ions. This substitution is more effective when the ion has a size and chemical behavior similar to that of the host ion it replaces.

Of particular interest in this thesis is the europium ion doped in to YSO, which has one of the narrowest homogeneous optical transitions of the rare-earth ions. YSO provides an exceptionally low magnetic background, which makes YSO a favorable host for reducing magnetic noise and narrowing the linewidth of the ions further (see Section 5.2 for more details).

3.2 Level structure of Eu:YSO

In the early 20th century, the Bohr model offered a bold new view of the atom: that electrons could only occupy specific energy levels, jumping between them by absorbing or emitting energy only in fixed amounts. This explained the sharp lines in the atomic spectra and marked a major break from classical physics. However, as the experiments became more precise, the limitations of the model became clear. That's when quantum mechanics stepped in, not to reject Bohr's idea, but to reshape it. It replaced fixed orbits with wavefunctions, blurry clouds of probability in which energy levels

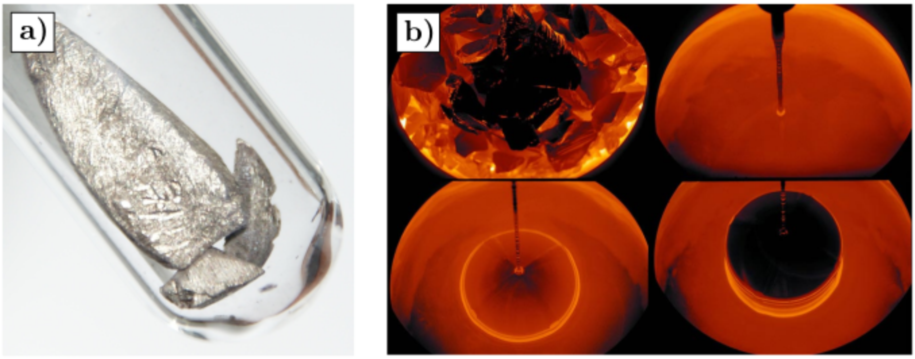

Figure 3.1: In a), a pure sample of Europium in a glass vial. Among the lanthanide elements, Europium stands out as the most chemically reactive, softest, and least dense. Its softness is such that it can be easily sliced with a knife.[31] In b), the Czochralski method demonstrating the process of dipping a rotating monocrystalline silicon seed crystal into molten silicon. As the seed crystal is pulled upward slowly, a cylindrical silicon monocrystal is formed.[32]

arise naturally from the mathematics of quantum mechanics, rather than being added in by assumption. In the quantum picture, not all transitions between energy levels are allowed, only those that obey specific rules tied to symmetries and conservation laws.[33,34]

These quantum rules dictate not only which transitions are allowed, but also hint at deeper layers of structure hidden within atomic energy levels. Energy levels can split into multiple closely spaced components.[35] This fine structure arises from interactions beyond the basic electron motion, specifically, the coupling between the electrons' angular momentum and the magnetic field generated by the nucleus. In this thesis, we are mainly interested in the electronic configuration of the trivalent europium ion RE^{3+} that has the form $[\mathrm{Xe}]4\mathrm{f}^6$. A defining feature of RE ions is the partially filled 4f electron shell, as these electrons have a radial distribution inside that of the filled 5s and 5p orbitals. Therefore, these ions become well shielded from the environment. In addition, electronic transitions within the 4f shell are not allowed for a free ion since parity is conserved (Laporte rule). However, when ions are doped into a crystal, the crystal field disturbs the orbital of the ion, so that the transitions become weakly allowed. The wavefunction describing the electron cloud effectively mixes in an opposite parity configuration due to the crystal field. Lastly, if the crystal is also cooled down to a few K, the density of phonons that contribute to the broadening of the line is greatly reduced. These effects all contribute to the very narrow linewidths (and long lifetimes) observed for rare-earth ions, and europium ions in particular. The long lifetimes of europium will be discussed in more detail in Ch. 4.

In Fig. 3.2 a), an illustrative diagram of the hyperfine structure of the ground state of europium in YSO is shown. Starting from the electronic configuration $4\mathrm{f}^6$, the energy levels are split due to free-ion interactions such as electrostatic Coulomb repulsion and spin-orbit coupling. Further splitting arises from ion-ligand interactions described by crystal-field theory. Nuclear electric quadruple interactions split the $J = 0$ crystal field singlets into three hyperfine levels ($I = \pm 1/2$, $I = \pm 3/2$, $I = \pm 5/2$). For electronic singlet states, the magnetic hyperfine interaction is quenched due to the absence of electronic angular momentum. Consequently, there is no first-order hyperfine splitting in these states.[35] In the presence of an external magnetic field, the degenerate quadrupole states are lifted into Zeeman levels.

For complete treatment of the hyperfine interaction including second order effects, the full Hamiltonian is often used to derive the energy level splittings[36,37]:

$$\mathcal{H} = \{\mathcal{H}_{FI} + \mathcal{H}_{CF}\} + \{\mathcal{H}_{HF} + \mathcal{H}_{Q} + \mathcal{H}_{z} + \mathcal{H}_{Z}\} \tag{3.1}$$

where $\mathcal{H}_{FI}$ is the contribution from the free ion including spin-orbit and Coulomb interactions, $\mathcal{H}_{CF}$ is the crystal field, $\mathcal{H}_{HF}$ hyperfine interaction, $\mathcal{H}_{Q}$ quadrupole, with $\mathcal{H}_{Z}$ and $\mathcal{H}_{z}$ representing the electronic Zeeman and nuclear Zeeman effect, respectively. The second group in Eq. 3.1 is then typically treated as a perturbation to the first. The hyperfine structure (quadrupole splittings) at zero magnetic field for the ground and excited states is shown in Fig. 3.2 b) for europium isotopes 151 and 153. Because YSO contains two inequivalent crystallographic sites for yttrium, this results in two distinct site locations for which the europium ion can substitute. The sites have different transition frequencies where the vacuum wavelength is $\lambda_{0,\mathrm{S1}} = 580.053\,\mathrm{nm}$ and $\lambda_{0,\mathrm{S2}} = 580.223\,\mathrm{nm}$ respectively. This thesis mainly concerns itself with site 1, as this site has larger absorption[40] and a narrower optical transition linewidth.[41]

Although the ions have very narrow individual absorption linewidths Γ_{h}, they obtain slightly different resonance frequencies when placed inside a crystal host. Because the ion does not perfectly match the atom it is replacing, there will be a slight irregularity in the crystal lattice, as can be seen in Fig. 3.2 c). This results in a spatially heterogeneous crystal

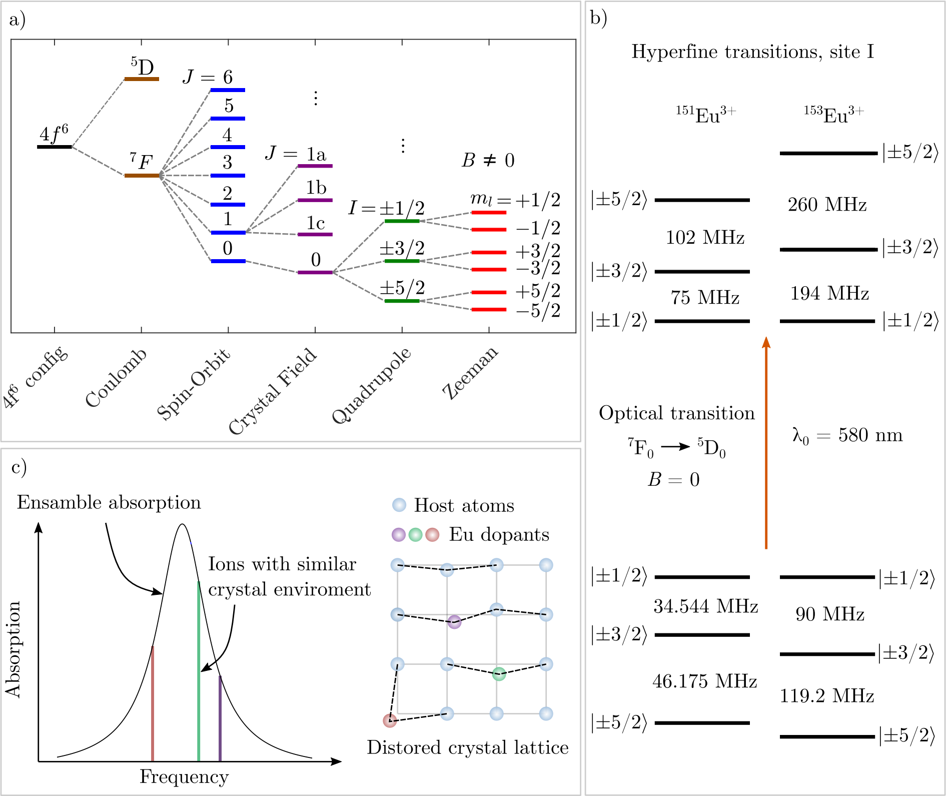

Figure 3.2: The hyperfine structure of Eu:YSO and inhomogeneous broadening effect. a), the splitting and corresponding mechanism starting from $4f^6$ (relative separations not to scale). The crystal-field-split sublevels have been labeled according to their respective total angular momentum (J) manifold as $J = 1\text{a}$, $J = 1\text{b}$, $J = 1\text{c}$ in the case of $J = 1$. In b), the optical and ground state hyperfine (quadrupole-split) sublevels as measured by ref.[38,39] In c), distortion in the crystal lattice resulting in inhomogeneous broadening.

field, which affects the transition frequency while still preserving the optical properties of the ion. The total effect of all ions in the crystal is an inhomogeneous broadening (Γ_{inh}) of the absorption profile, on the order of $\sim 10\,\text{GHz}$ (doping concentration dependent).[40] This is what allows for spectral tailoring of the absorption profile through optical pumping, which will be discussed next.

3.3 Optical pumping

When a narrowband laser is tuned to a specific frequency within the inhomogeneously broadened absorption profile, it selectively excites ions that are resonant with that frequency. Through a process called optical pumping, ions from a particular level are resonant with the laser and get repeatedly excited. Once excited, the ion can return to any of the ground states (including the level currently being pumped), according to the branching ratio. The ratio is the probability of deexcitation and can differ between levels. After some pumping time, the ions eventually move to the other ground-state hyperfine levels that are not resonant with the laser. As a result, the population of ions that absorb at the original frequency is depleted, creating a *spectral hole* in the absorption spectrum. The process is shown in Fig. 3.3. As more ions now reside in other hyperfine states these levels will have more than equilibrium absorption, the so-called *anti-holes*. The spectral hole (also referred to as a transmission window) and anti-holes reflect a redistribution of population among hyperfine levels from the equilibrium state. As the hyperfine relaxation lifetimes are very long, up to several weeks[42], the spectral features are effectively permanent. Because of inhomogeneous broadening, several ions will have transitions that are resonant at the same frequency. This is represented by the three ion classes in Fig. 3.3. However, this is a simplified case with only one excited state. In Eu:YSO there will be nine different ion classes per isotope resonant at any single frequency, as the excited state also has three levels.

The optical homogeneous linewidth of the ions will determine how narrow the spectral features can be made. For solids doped with rare-earth ions, the linewidth is composed of several different mechanisms:[40]

$$\Gamma_{\mathrm{h}} = \Gamma_0 + \Gamma_{\mathrm{ISD}} + \Gamma_{\mathrm{phonon}} \tag{3.2}$$

where Γ_{ISD} is the contribution from excitation induced dephasing (excitation density dependent), and where Γ_{phonon} is the broadening from coupling to phonons (temperature dependent). The phonon contribution can be greatly reduced by lowering the temperature of the ions to around 2 K using a cryostat. The minimum linewidth achievable is determined by the natural lifetime limit $\Gamma_0 = 1/(2\pi T_1)$ where T_1 is the relaxation lifetime of the excited state. For Europium, Γ_{h} has been measured to be $\sim 122\,\mathrm{Hz}$, closing in on Γ_0 at 81 Hz.[40]

In addition to the narrow linewidth of the ions, it is also necessary to use pumping pulses that are narrow in frequency to efficiently select ions in the

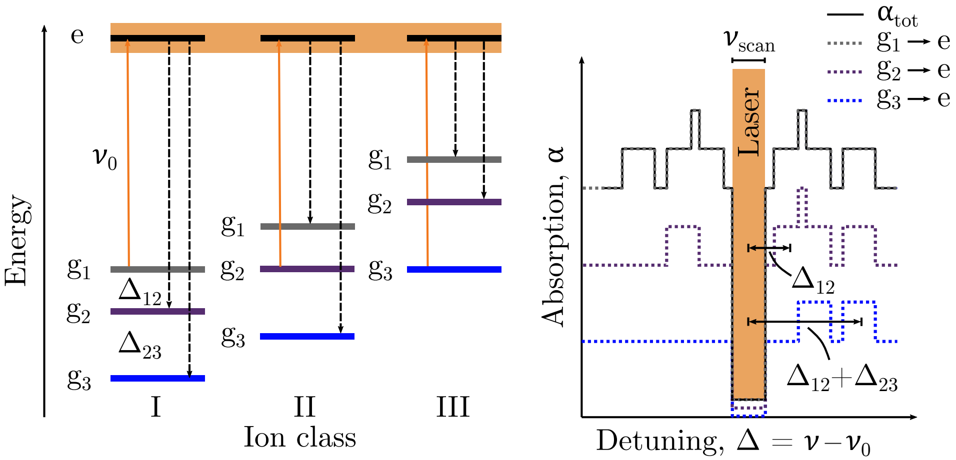

Figure 3.3: The optical pumping process for a simplified four-level system with three ion classes. Using a pumping frequency of ν_0 which is resonant with all three ions simultaneously, ions are brought to the excited state where they can de-excite again. De-excitation (dashed lines) can occur to any of the ground states, but if they fall down to the level being pumped they will be re-excited again. Eventually all of the population will reside in the other non-resonant ground states, which will see an increase in absorption. The increased absorption due to ion population at Δ_{12} and $\Delta_{13} = \Delta_{12} + \Delta_{23}$ have been notated for ion class I. These peaks will appear at all detunings however, including $\pm\Delta_{12}$, $\pm\Delta_{23}$, and $\pm\Delta_{13}$

inhomogeneous profile. To pump the transmission windows, we used complex hyperbolic secant pulses (or *sechyp*) and hyperbolic-square-hyperbolic (HSH) which we refer to as *sechscan*. The sechyp pulse was originally developed for nuclear magnetic resonance experiments[43], but found its way into other quantum information applications[44–46] as it was shown to be capable of fully inverting a population coherently without being sensitive to absolute intensity. The sechscan pulse extends the effective frequency width of a sechyp by adding a square-amplitude pulse with a linearly chirped frequency between two halves of a sechyp pulse.[47]

Chapter 4

Resetting the hyperfine structure using RF fields

Rare-earth-ion-doped crystals have emerged as indispensable platforms in quantum information science owing to their combination of narrow optical transitions and long-lived hyperfine states. Among these, europium-doped yttrium orthosilicate (Eu:YSO) is particularly noteworthy for its exceptionally long hyperfine coherence and population lifetimes. Eu:YSO offers ground-state hyperfine coherence times extending from hours to beyond 10 hours under special "ZEFOZ" conditions[48], and hyperfine state lifetimes on the order of weeks[42] at cryogenic temperatures. Such extended lifetimes are a double-edged sword: they enable applications like laser stabilization, quantum memories with truly persistent storage, and qubit gates, but they also pose challenges for device reusability and state initialization. Once hyperfine populations are optically pumped or spectrally tailored (as in hole-burning-based quantum memory protocols[49] and slow light laser stabilization[50]), the induced spectral features and population imbalances can persist for extremely long durations, unless an active reset mechanism is employed. The long-lived nature of Eu^{3+} nuclear spin states means that, after spectral manipulation, residual spectral holes or inverted populations can linger and degrade subsequent experiments via residual (or lack thereof) absorption. This motivated the study of **Paper II**: developing efficient techniques to *reset* or re-equilibrate long-lived hyperfine populations in Eu:YSO, thereby fully capitalizing on its advantages for quantum information processing.

Resetting hyperfine populations in rare-earth doped materials is nontrivial. The straightforward approach of thermal cycling (warming the crystal to accelerate spin relaxation) is impractical for rapid, repeated operation. While raising the temperature to tens of kelvin can collapse Eu:YSO hyperfine lifetime from weeks to seconds, it disrupts cryogenic stability and incurs significant downtime. Optical erasure techniques have been explored as well: for example, using broadband or frequency-chirped laser pulses to optically excite ions and redistribute populations among ground states through relaxation processes. However, this is not energy efficient, as we will see in the next section. Therefore, a more energy efficient approach is needed to reset hyperfine state populations.

In this chapter, we explore the application of radio-frequency (RF) magnetic fields to actively reset hyperfine-level populations. By resonantly driving the hyperfine transitions in the ground state, an RF field can re-equilibrate the spin populations in situ without heating the crystal. In principle, a sufficiently strong RF drive can induce rapid transitions between all hyperfine sublevels for all ions, scrambling the stored nuclear spin order, and returning the ensemble to an effective thermal mixture. In **Paper II** we demonstrate this concept in Eu:YSO, using a highly tunable resonant RF transmitter coil circuit to address multiple hyperfine transitions and effectively erase persistent spectral hole features. The circuit needs to be highly tunable as the hyperfine separation in the ground state in Eu : YSO is large ($> 100\,\mathrm{MHz}$). This is greater than that of praseodymium, which has hyperfine splittings on the order of a few tens of MHz.[51] The design of the cryogenic tunable transmitter coil is described in **Paper I**. Unlike optical erasure, the RF approach can target the nuclear degrees of freedom directly, which offers significant efficiency advantages because of the quasi-equilibrium state of a majority of ions in the material. Because most ions remain in an equilibrium state, the material appears nearly transparent to RF fields, resulting in minimal net energy absorption and reduced heating. In contrast, optical erasure methods require broad spectral coverage and often induce population inversion, leading to increased nonradiative relaxation and potential lattice heating. Thus, RF-erasure offers a clear advantage in leveraging the long hyperfine lifetimes of Eu:YSO for state initialization. For slow light laser stabilization (**Paper III** & **Paper V**) it was used to reset transmission windows after degradation of the locking beam (see Section 5.3.4). This allowed us to perform subsequent locking at the same frequency to retain good locking conditions.

4.1 Fundamental energy efficiency for RF erasure

The efficiency of resetting hyperfine populations using radio-frequency (RF) fields benefits from the quasi-equilibrium state of a majority of ions within the material. Since most ions remain thermally distributed among the hyperfine levels, the material appears nearly transparent to the applied RF fields. This transparency arises because the probability of stimulated emission is almost equal to that of absorption, resulting in no net energy transfer to the ions. Consequently, no significant heating of the material should occur as energy is neither absorbed nor released through ion-lattice interactions. Instead, any joule heating observed is solely due to resistive losses and imperfections in the RF circuit itself.

The efficiency of resetting hyperfine populations using radio-frequency (RF) fields benefits from the quasi-equilibrium state of the majority of ions in the material. Since most ions remain thermally distributed among the hyperfine levels, the material is effectively transparent to the applied RF fields. This apparent transparency arises because the probabilities of stimulated absorption and emission are nearly equal, leading to no net energy transfer to the ions. As a result, the RF field does not cause additional heating, since energy is neither accumulated in the ions nor supplied to sustain non-radiative decay into the lattice.

The power dissipated in the circuit as heat is P_{diss} and on resonance $P_{\text{diss}} = P_{\text{in}}$. The circuit will then be purely resistive, so that $P_{\text{diss}} = RI^2$ where R is the equivalent resistance in the circuit and I is the current. Thus, to reduce Joule heating, we want to reduce R of the circuit. This is a technical limitation rather than a fundamental one. With a lossless superconducting resonance circuit, no heat would be dissipated. It is, of course, still a challenge to design such a circuit and still maintain the high and flexible tuning capability required for erasure in Eu:YSO. These design constraints are discussed in more detail in **Paper I**.

In contrast, the optical erasure method requires significantly more energy to achieve a uniform redistribution of ions across the hyperfine states. The total energy required for optical erasure, E_{opt}, can be estimated as:

$$E_{\text{opt}} = h\nu \times N_{\text{ions}} \times n_{\text{scan}}, \tag{4.1}$$

where h is Planck's constant, ν is the optical transition frequency, N_{ions} is the total number of ions, and n_{scan} is the number of scans needed to efficiently erase the spectral features. Optical erasure often involves broad spectral scanning due to the inhomogeneous broadening of the optical transitions, resulting in higher energy requirements. Using realistic values for our cavity: $N_{\text{ions}} \approx 400 \times 10^{18}$, $\nu \approx 500$ THz and $n_{\text{scan}} \approx 5$ the resulting energy is about $E_{\text{opt}} = 663$ J, or close to 10^2 times as much energy as for RF erasure.

The RF erasure technique offers a highly efficient method to reset hyperfine populations with minimal heating, primarily limited by the quality of the RF circuitry. The next section will describe the design used in the experiments in more detail.

4.2 Design of a cryogenic tunable resonant RF-coil (Paper I)

The main goal of the design, described in **Paper I**, was to fabricate a device that could produce strong magnetic fields resonant with the transitions in Eu:YSO. However, since our experiments were performed around 1.5 to 2 K inside a cryostat, this adds additional constraints on efficiency to avoid cryostat heating. The initial idea was to use a RLC resonance circuit with some form of tunable element where L represents a magnetic field generating coil and C the tunable capacitance. Resonance circuits are typically compact and power efficient as most power can be delivered within a narrow band of frequencies. If the resonator is also made with low resistance materials and components, heat generation can be minimized (as we saw in Section 4.1) while peak current is maximized.[52]

High currents I are required to generate a strong magnetic field B in a RLC circuit, as $B \propto NI$ where N is the number of turns of the coil. The maximum current amplitude in the resonator is given as

$$I_{\text{max}} = \frac{V_{\text{coil}}}{X_{\text{coil}}} = Q\frac{V_{\text{in}}}{X_{\text{coil}}} \tag{4.2}$$

where V_{coil} is the voltage across the coil, V_{in} the input and X_{coil} the reactance of it, and V_{in} the input voltage. The Q-factor represents how efficient the circuit is at storing energy,

$$Q = X_{\text{coil}}/R \tag{4.3}$$

which is also dependent on the coil reactance so that the resulting maximum current is determined by

$$I_{\text{max}} = V_{\text{in}}/R \tag{4.4}$$

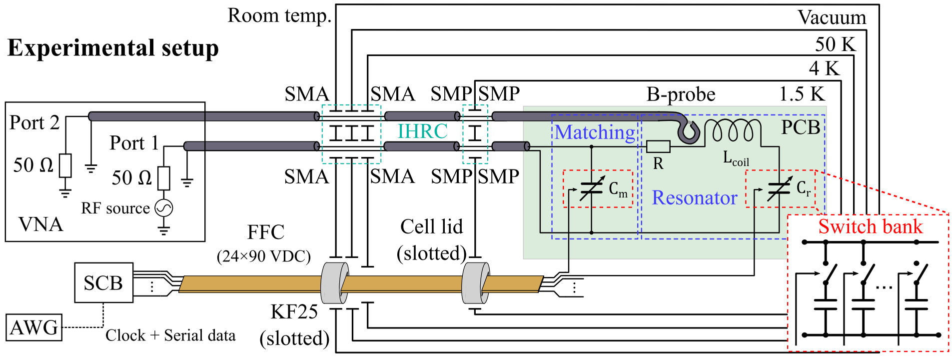

Figure 4.1: The experimental setup for characterizing the RF resonance circuit. The circuit was probed with a network network analyzer at port 1, with the magnetic field measured at port 2 using a magnetic field probe. Tuning was done through capacitance switch banks, controlled via a switch control board (SCB).

Thus, to maximize the magnetic field the resistance of the resonator should be minimized. However, for the purpose of our objective to reset the population in Eu:YSO, minimizing R had to be secondary to obtaining the full tuning range, as it is critical to be able to reach every necessary transition for a full reset. As can be seen in Fig. 3.2 b), the largest ground state hyperfine splitting is 119 MHz while the smallest is 34.5 MHz. The motivation for materials and components of the circuit that meet these requirements is discussed further in Section 4.2.1.

The tunable resonant coil transmitter design used to reset the population in Eu:YSO at 1.5 K is shown in Fig. 4.1. The circuit consists of a RLC resonator and the matching network and utilizes in situ tuning for both the matching capacitance C_m and resonator capacitance C_r. Tuning is performed using commercially available high-power MEMS switch capacitor banks that are controlled via applying a DC bias. Magnetic fields were measured using a B probe in close proximity to the coil to characterize the circuit performance.

The following sections will discuss the performance of the circuit in general as well as describe the function of matching, tuning capabilities, and magnetic field generation efficiency for the transmitter coil in more detail.

4.2.1 Components and material selection

To obtain a large tuning range we considered a few options including varactors, switches, and a combination of both in addition to device materials suitable for cryogenic operation. Starting with materials, Eq. 4.4 will naturally bring the attention to superconductors.

Tuning using superconductors has been demonstrated for receiver coils in, for example, high temperature superconductors (HTS) coils for MRI using inductive coupling[53], high-Q filters using mechanical superconducting microelectromechanical systems (MEMS) switches[54,55] and quantum interference devices (SQUIDs) that are tuned with magnetic flux[56]. Although these devices often have very high Q-values, their tuning range is often limited to a few percentages. Furthermore, these designs are often not commercially available, which means that they would have to be produced in-house.

As we were looking for a much larger tuning range for a transmitter coil configuration, some commercially available options like direct band gap varactors and MEMS switches had the tuning range required. Direct band gaps are required due to the electron freeze-out effect at cryogenic temperatures[57], which is also why conventional silicon complementary metal oxide semiconductors (CMOS) components are generally not viable. Initial designs used back-to-back configuration of GaAs varactors (see for example Schubert[58] or Koivuniemi[59]) and were simulated in *LTSpice* for maximum current and tunability. By applying a DC voltage to the varactor, the width of the depletion region can be changed, resulting in a shift of capacitance. This approach offers continuous tuning with one large drawback being resonator stability, as the AC component in the RF field across the varactor can change its capacitance and therefore induce harmonics in the resonator. Larger tuning ranges typically mean a higher non-linear response, which limits the maximum power that can be used.

As we needed higher power for stronger magnetic fields in the transmission coil, we opted for mechanical switches instead using a switch-bank configuration. The switch (Menlo Micro, 5130) could withstand high voltages (100 V) and had a 0.1 dB (1.1 Ω) insertion loss at 1 GHz. These switches have been characterized for reliability in a cryogenic environment down to 55 K in a previous study.[60] At 50 K the contact resistance from a four point measurement was about 2 Ω (so higher than room temperature). The extrapolated value at 1 K is about 1 to 1.5 Ω, similar to room temperature.

The five turn transmission coil (see Fig. 5.7) was made from oxygen-free copper (Luvata, OFE-OK), because this allows for very low resistance at cryogenic temperatures. The coil had a Residual Resistivity Ratio (RRR) of 400, which resulted in very low resistance. The RRR is defined as the ratio between a material's resistivity at room temperature and its resistivity at absolute zero (or the nearest achievable temperature):

$$RRR = \frac{\rho_{300\,\mathrm{K}}}{\rho_{0\,\mathrm{K}}} \tag{4.5}$$

The switches were still the limiting factor for resistance so in principle one could have used a lower electronic grade copper.

Finally, the capacitors used were ceramic of type C0G/NP0 with low equivalent series resistance (ESR) around 0.1 to 0.2 Ω. These capacitors have a very stable dielectric response at cryogenic temperatures.[61]

4.2.2 Matching the circuit

In a regular *RLC* resonance circuit, the load impedance is purely real (resistive) on resonance due to the reactance of L_{coil} and C_{r} being equal in magnitude but opposite in phase. Because we are trying to keep the equivalent series resistance R low, there will generally be an impedance mismatch, since the input impedance of a transmission line is usually chosen to be 50 Ω. This can lead to significant signal reflections at the interfaces where the cable connects to the resonance circuit, resulting in only a small part of the power being transferred.

To reduce reflections, it is necessary to add a matching network to the circuit to match the input impedance. Impedance matching should ideally be performed in situ, inside the cryostat, rather than externally. If matching is conducted outside the cryostat, the connecting cables themselves become part of the resonant circuit loop. This configuration leads to increased resistive losses (Joule dissipation) and undesired RF interference.[52] These cables typically have low thermal conductivity (and therefore high resistive losses) to not thermally load the cryostat. Thus, placing the matching network as close to the resonance circuit as possible significantly reduces resistive losses and avoids loading the circuit. Some examples of in situ matching are passive matching designs using trimmer capacitors[52] or inductive coupling[62,63], and direct bandgap varactors[58,59]. Passive matching designs require setting the matching at room temperature, which can be problematic as matching conditions change at cryogenic temperatures.

Varactors with large tuning ranges typically have a non-linear response, resulting in harmonics being generated in the resonance circuit, limiting the input power.[58]

The main motivation for using mechanical switches in our experiments was the higher power handling (for resonance frequency tuning) and predictable behavior (for matching tuning) at cryogenic temperatures. In order to increase the impedance of the resonance circuit to match the source impedance Z_s, we can add a single capacitor parallel to the circuit C_m. In our case, C_m is tunable through the capacitor bank. The total input impedance given by this parallel combination is:

$$Z_\mathrm{in}(\omega) = \underbrace{\Big(R + jX_\mathrm{LC}\Big)}_{\text{RLC resonator}} \Big\| \underbrace{\Big(-jX_\mathrm{m}\Big)}_{\text{matching capacitor}} \tag{4.6}$$

$$= \frac{X_\mathrm{LC}X_\mathrm{m} - jRX_\mathrm{m}}{R + j(X_\mathrm{LC} - X_\mathrm{m})}. \tag{4.7}$$

For impedance matching at resonance, we need:

$$\mathrm{Im}[Z_\mathrm{in}(\omega)] = 0, \tag{4.8}$$

$$\mathrm{Re}[Z_\mathrm{in}(\omega)] = Z_\mathrm{s} \tag{4.9}$$

These will be the best match conditions (maximum power transfer) so that $X_\mathrm{m} = X_\mathrm{m,opt}$. Thus, separating the real and imaginary parts of $Z_\mathrm{in}(\omega)$, we find the following constraints:

$$X_\mathrm{m,opt}[X_\mathrm{LC}^2 + X_\mathrm{LC}X_\mathrm{m,opt} + R^2] = 0 \tag{4.10}$$

$$\frac{RX_\mathrm{m,opt}^2}{R^2 + (X_\mathrm{LC} - X_\mathrm{m,opt})^2} = Z_\mathrm{s} \tag{4.11}$$

where $X_\mathrm{m,opt} \neq 0$ is assumed. Solving Eq. 4.10 for X_LC yields two possible solutions,

$$X_\mathrm{LC} = \frac{X_\mathrm{m,opt} \pm \sqrt{X_\mathrm{m,opt}^2 - 4R^2}}{2}. \tag{4.12}$$

where the relevant solution is the (+) branch, which corresponds to stepping up the small R to a larger Z_s. This ensures that the net reactance remains near resonance, as $X_\mathrm{LC} \approx X_\mathrm{m,opt}$, if $R \ll X_\mathrm{m,opt}$. Substituting Eq. 4.12 into Eq. 4.11 we can express the matching capacitance $X_\mathrm{m,opt}$ as

$$X_\mathrm{m,opt} = \frac{Z_s}{\sqrt{\frac{Z_s}{R} - 1}}. \tag{4.13}$$

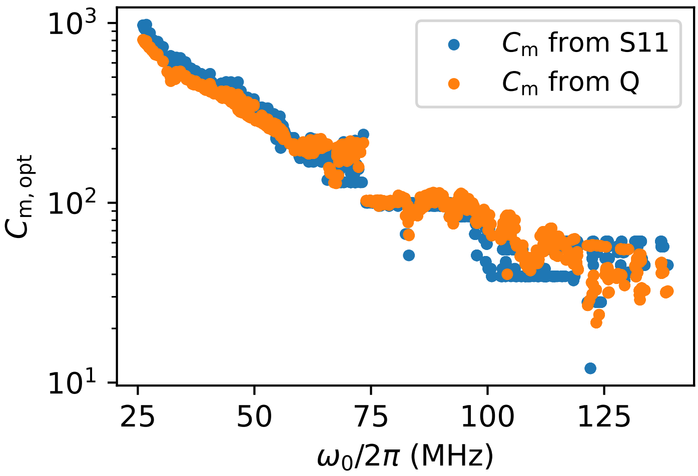

Figure 4.2: The perfect matching capacitance $C_{\mathrm{m,opt}}$ measured either directly through S11 or indirectly via the Q-value of the magnetic field resonance peak.

or equivalently, solving for the best match capacitance $C_{\mathrm{m,opt}}$, performing some algebraic rearrangement,

$$C_{\mathrm{m,opt}} = \frac{\sqrt{Z_s - R}}{\omega Z_s \sqrt{R}} \tag{4.14}$$

By substituting R using Eq 4.3, $C_{\mathrm{m,opt}}$ can be calculated from the Q value of the circuit (by measuring Q at the peak magnetic field) or obtained directly by recording the value C_{m} where the reflected signal (S11) is at minimum. The result of this comparison is shown in Fig. 4.2.

A side effect of adding a matching parallel capacitor is that the matching capacitor effectively "pulls" the resonator away from its natural series resonance.[52] Physically, this occurs because the additional reactance of the matching capacitor shifts the frequency at which the impedance transformation occurs. Instead of operating precisely at the bare resonance of the resonator, the system finds a new balance where the total reactance cancels and the impedance transformation to Z_s is achieved. The shift is dictated by the loading effect of X_{m}, which modifies the effective reactance seen by the source.

This behavior can be exploited to fine-tune the circuit using only the matching capacitance. As long as we stay close to the conditions given by Eqs.

4.9 and 4.8, small adjustments in C_m allow us to change the resonance frequency without significantly degrading the matching. An added benefit of this is that we can avoid *hot-switching* of the resonance capacitance (tuning of C_r while simultaneously sending in RF power), as this can damage the switch. Because the voltage across the matching capacitor C_m is low compared to C_r inside the resonator, there is generally no issue in tuning C_m during operation.

Nevertheless, in most cases the optimum match configuration $\omega_0 \approx \omega$ so that we can ignore the shift caused by the matching capacitor. In the next section, we shall see how switch bank resonator tuning works using C_r as well as how C_m can be used for fine adjustments of the resonance frequency.

4.2.3 Resonator and matching capacitance tuning

The circuit was designed to reach the necessary transitions for both isotopes $\left({}^{151/153}\mathrm{Eu}\right)$ including $|\pm 1/2\rangle_g \leftrightarrow |\pm 3/2\rangle_g$ and $|\pm 3/2\rangle_g \leftrightarrow |\pm 5/2\rangle_g$ in order to move the population between levels. Using capacitor switch banks, it is possible to create a semi-continuous frequency tuning range if the steps in capacitance can be made small, as demonstrated in Fig. 4.3. Although we did not necessarily need this detail of tuning, it made the circuit more general-purpose for use in other applications.

The driven bare resonance frequency ω_0 measured are given by

$$\omega_0 = \frac{1}{\sqrt{LC}} \tag{4.15}$$

where $L \approx L_\mathrm{coil}$, $C \approx C_\mathrm{r}$, and $\omega_0 \approx \omega$ are assumed. The inductance of the circuit (dominated by the coil) was measured to be $0.33\,\mu\mathrm{H}$. Simulations in *COMSOL* for the coil geometry ($N = 5$, $a = 17\,\mathrm{mm}$, $b = 16\,\mathrm{mm}$, $l = 20\,\mathrm{mm}$, $d = 1\,\mathrm{mm}$) resulted in an inductance of $L_\mathrm{coil} = 0.31\,\mu\mathrm{H}$. A fit of ω_0 suggested a parasitic capacitance of $C_\mathrm{p} \approx 4.4\,\mathrm{pF}$.

As mentioned above, C_m can be used to shift the resonance frequency ω of the circuit. However, moving too far from $C_\mathrm{m,opt}$ will degrade the matching. The matching conditions can be measured with a vector network analyzer (VNA)(V2/SAA2, NanoRFE) through the reflection coefficient S11 which measures the return loss of a device, indicating how much of the input power supplied to the device reflects back to the input port. Fine tuning of ω for the magnetic field (and S11) is demonstrated in the inset of Fig. 4.3, where C_m was stepped around $C_\mathrm{m,opt}$. This gives an extra degree of

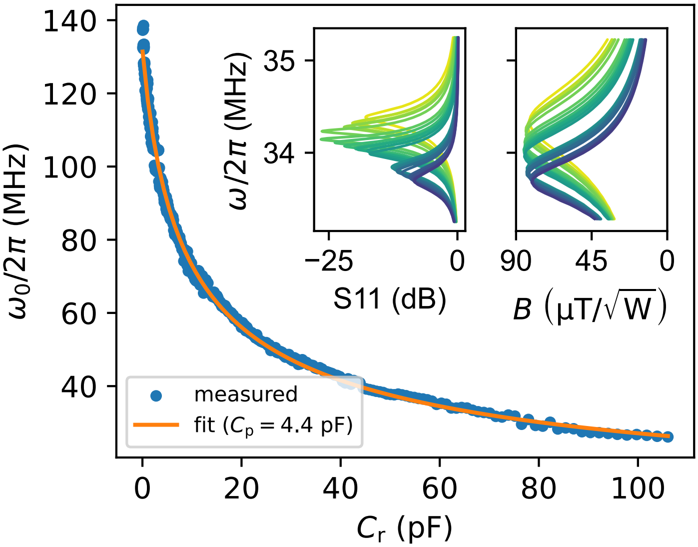

Figure 4.3: Tuning performance of the resonance circuit. Resonance tuning using capacitor switch banks, following Eq. 4.15. The inset figure shows fine tuning of the magnetic field using matching switches.

freedom for tuning which can be used to obtain continuous tuning of the magnetic field resonance frequency, as will be shown in the next section.

4.2.4 Transmitter coil field generation

To measure the magnetic field, we connected a single-turn B field probe to the second port of a VNA (see Fig. 4.1). The transmission coefficient S21 measured by the VNA can then be related to the magnetic field B if the probe is calibrated correctly. The single loop magnetic RF probe was constructed using a $50\,\Omega$ coaxial cable and designed to match the square cross-sectional area of the coil. Prior to installation in the cryostat, we performed a relative calibration against a factory calibrated magnetic field probe (Tekbox, TBPS01 H10) to establish a relationship between the transmission coefficient S21 and the magnetic field via a calibration factor, $\Delta_{\mathrm{cal}}(\omega)$. The magnetic field generation efficiency is then determined by

$$B_{\mathrm{eff}} = \frac{B_0}{\sqrt{P_0}} 10^{(\log_{10}(|S21(\omega)|) - \Delta_{\mathrm{cal}}(\omega)/20)} \tag{4.16}$$

with B_0 and P_0 referenced at 1 µT and 1 mW respectively, so that the unit of B_{field} is $\mu\text{T}/\sqrt{\text{W}}$. This effectively represents how well the circuit converts an RF input power P_0 to a magnetic field in the coil.

As the magnetic field probe was placed 13 mm from the center of the coil to not load the circuit, the magnetic field seen by the probe can be substantially reduced. Compensating for this effect meant that we had to estimate what the equivalent field was in the center of the coil. Below I derive an expression for the magnetic field given a square coil geometry with side lengths $a \neq b$.

The magnetic field at a point due to a differential current element Idl is given by:

$$\mathrm{d}B = \frac{\mu_0 I}{4\pi} \frac{\mathrm{d}l \times \boldsymbol{r}}{|\boldsymbol{r}|^3} \tag{4.17}$$

where I is the current, dl the differential length element, and $\boldsymbol{r}$ the vector from the current element to the point where the field is being measured. For a rectangular coil, we can consider four element segments (-a/2, y), (a/2, y), (x, -b/2), and (x, b/2) which will have pairwise symmetry. To a point $(0, 0, z)$ on the z-axis the position vector is given by $\boldsymbol{r} = (-x_{\text{seg}}, -y_{\text{seg}}, z)$ and the segment differential is $\mathrm{d}l = (\pm\mathrm{d}x, \pm\mathrm{d}y, 0)$. For segments parallel to the x-axis (at $y = \pm b/2$) the magnetic field along the z-axis can be estimated as:

$$B_{\text{z,x}} = \frac{\mu_0 I b}{8\pi} \int_{-a/2}^{a/2} \frac{\mathrm{d}x}{(x^2 + (b/2)^2 + z^2)^{3/2}} \tag{4.18}$$

and segments parallel to the y-axis (at $x = \pm a/2$) have:

$$B_{\text{z,y}} = \frac{\mu_0 I a}{8\pi} \int_{-b/2}^{b/2} \frac{\mathrm{d}y}{(y^2 + (a/2)^2 + z^2)^{3/2}} \tag{4.19}$$

Solving the integral and summing the contributions from all the segments, I obtain:

$$B_{\text{z}} = \frac{\mu_0 I ab}{4\pi} \left(\frac{1}{A\sqrt{(b/2)^2 + A}} + \frac{1}{B\sqrt{(a/2)^2 + B}} \right) \tag{4.20}$$

where substitutions have been made for $A = (a/2)^2 + z^2$ and $B = (b/2)^2 + z^2$.

Considering a coil with N turns, the loops will be located at different observation points $z_{\text{obs}} = z - z_i$ so that the field becomes

$$B_{\text{z}} = \frac{\mu_0 I ab}{4\pi} \sum_{i=1}^{N} \left(\frac{1}{A\sqrt{(b/2)^2 + A}} + \frac{1}{B\sqrt{(a/2)^2 + B}} \right) \tag{4.21}$$

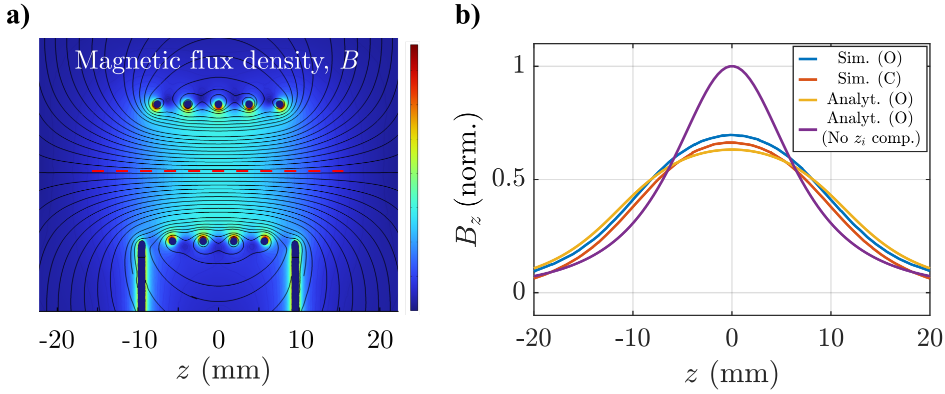

Figure 4.4: Field homogeneity inside the cell for a non-resonant rectangular coil. In a), the simulated magnetic flux density from a center cross section. The magnetic field homogeneity along a center line (dashed line in a)) is shown in b) for different cases. The cases are simulated field given an open environment of vacuum (blue), closed environment inside the cryostat 1 K cell (orange), the analytical calculated values with (yellow) and without (purple) accounting for individual turn distances.

with $A = (a/2)^2 + z_{\text{obs}}^2$ and $B = (b/2)^2 + z_{\text{obs}}^2$.

In addition to the analytical expression for the field along the z-axis, we were also interested in the homogeneity of the resulting volume field. The simulated magnetic flux density for this coil is shown in Fig. 4.4 a) where the center z-axis has been marked with a dashed line. A comparison between simulations and the analytical expression (Eq. 4.21) is shown in Fig. 4.4 b). Two cases were simulated: cell enclosing (C) including the cryostat 1 K cell and open (O) with just a vacuum environment. This was done because the magnetic field, B_{z}, at the probe position is expected to be further reduced due to shielding effects from the copper cell. Two analytical cases were also included for the open cell case, where we either account for the different observations of the coil turns or exclude this effect.

The simulation results show that the cell reduces the field, on the order of 10 to 15 %. Furthermore, the analytical expression using observation point compensation seems to fit the simulations well (blue and yellow trace). However, a slight underestimation of the field is done for the center of the coil.

Using a combination of resonator and matching tuning, a large number of resonance frequencies for the magnetic field can be obtained. By overlapping multiple resonance peaks across a wide frequency range, we can generate a continuous magnetic field if each peak is allowed to be detuned slightly. Each resonance peak has a specific bandwidth where the magnetic field remains within 3 dB of its maximum value, and this bandwidth is determined by the Q-factor. Higher Q-factors result in narrower bandwidths, requiring a higher density of resonance peaks to maintain continuous tuning. Conversely, lower Q-factors allow for broader bandwidths, reducing the number of resonances needed for overlap. This creates a trade-off between achieving a seamless tuning range and maximizing the peak magnetic field strength. Magnetic field generation efficiency was evaluated using points evenly spaced in frequency throughout the frequency range with a resolution of 11.3 kHz. At each frequency point, all resonance peaks in the vicinity were analyzed to determine the maximum achievable magnetic field. The curve corresponding to the highest magnetic field was then selected at each evaluation point. The result is presented in Fig. 4.5 a). The corresponding Q-factor, C_m, and C_r for the selected curve is shown in panels b), c) and d), respectively.

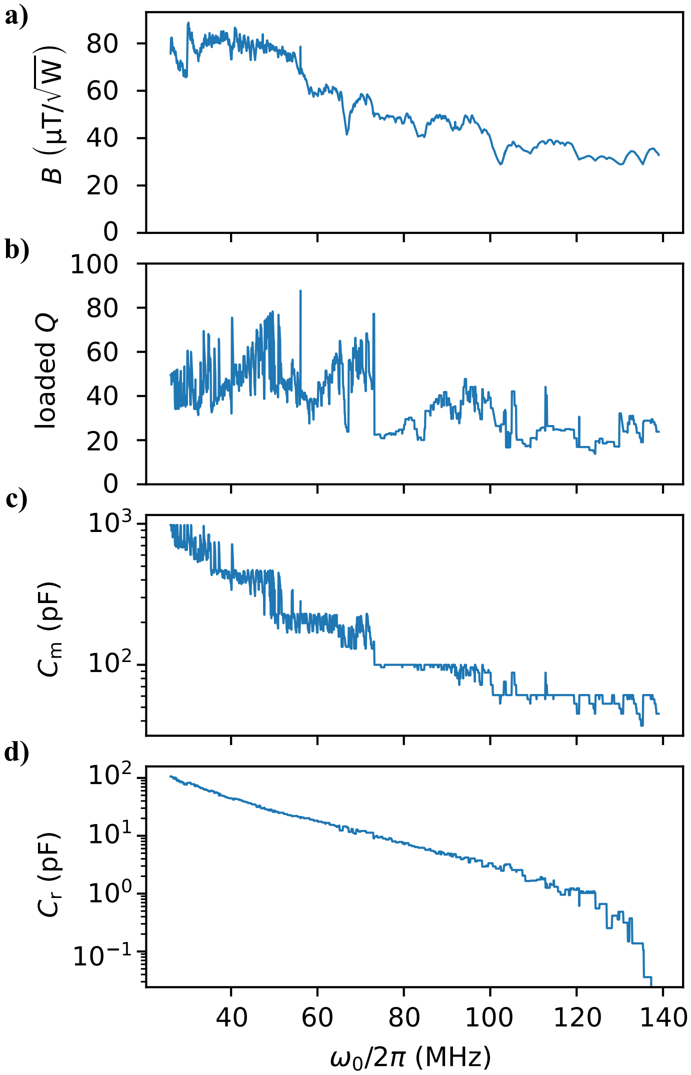

Figure 4.5: Circuit tuning and magnetic field characteristics. In a), Magnetic field generation efficiency over the 25–$140\,\mathrm{MHz}$ frequency range. The magnetic field amplitude at each frequency was determined by identifying the maximum magnetic field among nearby resonance peaks within a $3\,\mathrm{dB}$ bandwidth window. Frequencies were sampled at uniform $11.3\,\mathrm{kHz}$ intervals. Slight detuning of resonances allows overlap between adjacent magnetic field curves, resulting in a continuous magnetic field generation profile. b), loaded Q-factor corresponding to the magnetic field data in a). c), switch bank matching capacitance and (d) resonance tuning capacitance associated with each frequency point.

4.3 Resetting long-lived ground states in Eu:YSO (Paper II)

We have demonstrated a method for a full population reset by showing that we can effectively swap populations between all hyperfine states. Because the RF pulses uniformly affect all ions across the inhomogeneous profile, it is sufficient to demonstrate population reset within a narrow spectral region. We therefore choose to burn transmission windows (from now on abbreviated TW) locally as this is a simple structure where the contrast in absorption can tell us how much of the population has returned to the hole after applying RF-pulses.

As we have seen in Ch. 3, optical pumping will cause ions to move between the hyperfine ground states, emptying their original state.[64] Due to the inhomogeneous broadening in Eu:YSO, there will be nine different classes of ions per isotope that can be situated in any of the hyperfine ground states for a given frequency. The goal is to use RF pulses, resonant with the hyperfine transitions, to evenly redistribute the ions across all hyperfine levels and reverse the population imbalance caused by optical pumping. **Paper II** describes the methodology for this type of population reset.

To simplify the discussion of how to efficiently mix populations, we begin by considering just two levels. By fully mixing these levels, we mean creating a statistical mixture in which the system has equal probability of occupying either state. This corresponds to an equal population distribution without coherence between the levels. This state resembles that of a thermal equilibrium distribution with equal populations, as would occur at high temperatures. However, in this case, the equal population is not the result of thermalization but is instead actively prepared through population mixing.

To demonstrate level mixing using RF pulses, it may be helpful to introduce the Bloch sphere (shown in Fig. 4.6), which is a geometric representation that provides an intuitive way to describe the state of a two-level system.[65,66] Any state of the two-level system can be mapped to a point on or inside this sphere. The state of the system is typically expressed in terms of a three-component vector, known as the Bloch vector, which determines the position on the sphere. This Bloch vector is given by

$$\vec{r} = (\sin\theta\cos\phi,\ \sin\theta\sin\phi,\ \cos\theta) \tag{4.22}$$

where r, θ and ϕ are the spherical coordinates. The length of r will then determine the *purity* of the state, ranging from $r = 1$ for a pure state (on the surface of the sphere) to $0 < r < 1$ for a mixed state (inside the sphere) and reaching $r = 0$ for a maximally mixed state (at the center). The polar angle θ, which varies between $0 \leq \theta \leq \pi$, determines the population distribution between the basis states $|g_1\rangle$ and $|g_2\rangle$, with $\theta = 0$ corresponding to $|g_1\rangle$ and $\theta = \pi$ corresponding to $|g_2\rangle$. The azimuthal angle ϕ, which ranges from $0 \leq \phi < 2\pi$, defines the phase relationship between the two basis states.

The longitudinal lifetime represents the decay rate between $|g_2\rangle$ and $|g_1\rangle$. This type of decay is thus described by the polar angular rate $\dot{\theta}$, with an evolution of the Bloch vector that occurs in the longitudinal plane, as shown in Fig. 4.6. The dephasing rate is, on the other hand, described by dephasing processes in the transverse plane. As mentioned in the beginning of the chapter, Eu:YSO has hyperfine lifetimes (longitudinal decay rate) that are extremely long. Although long coherence times (transverse decay rate) have been achieved in Eu:YSO, it is generally of the order of a few ms without applying external magnetic fields.[67,68] Since longitudinal decay occurs over several weeks, the decay rate varies by several orders of magnitude.

The idea here is to move ions from the longitudinal plane where the relaxation process is slow, to the transverse plane where relaxation occurs in a few ms. In practice, this means that we need to move the population from both poles of the Bloch sphere coherently to a superposition state on the equator, so that the Bloch vector is rotated by $\theta = \pi/2$. This type of operation is therefore usually called a $\pi/2$-pulse when the transition is driven externally. After applying a $\pi/2$-pulse, the ensemble of ions will start to dephase relative to each other and spread out on the equator. However, due to decoherence the state will also start to decay towards the center of the sphere, creating a mixed state. This process of resetting the population is shown in Fig. 4.6 b) to c). We can describe the mixed end state by first considering the ions that initially reside in $|g_1\rangle$. Applying a coherent $\pi/2$ pulse, we rotate the Bloch vector from $|g_1\rangle$ to the equator. As ϕ can be chosen arbitrarily, we set $\phi = 0$. The Bloch vector then becomes $\vec{r}(0) = (1, 0, 0)$, pointing in the x-direction.

After the pulse, suppose each ion undergoes phase evolution while remaining on the equator (i.e. $\theta = \frac{\pi}{2}$) but with a time-dependent azimuthal angle. For the i-th ion, assume:

$$\phi_i(t) = \omega_i t,$$

where ω_i is the ion-specific angular frequency. The Bloch vector for ion i

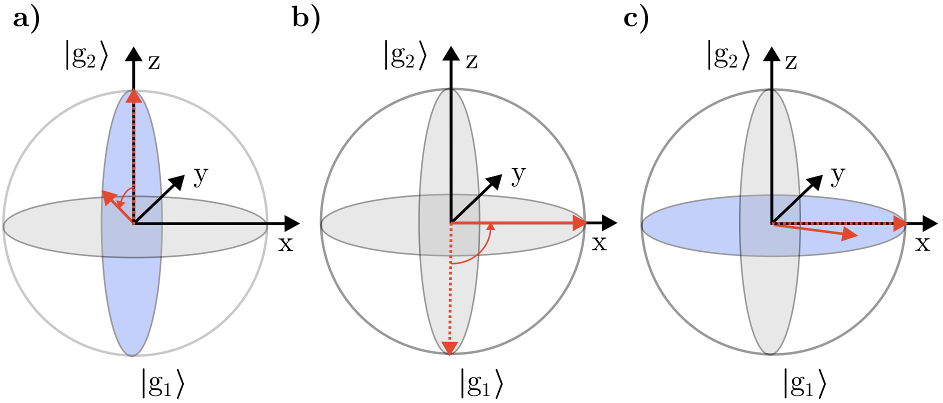

Figure 4.6: Process of resetting a state to thermal equilibrium. Resetting the population to equilibrium involves rotating the state away from the longitudinal plane (a) to the equatorial plane where it becomes susceptible to rapid dephasing (c). This can be achieved by applying a coherent $\pi/2$-pulse (b), which leads to thermal equilibrium as the state vector start to shrink towards the center of the sphere.

is then:

$$\vec{r}_i(t) = e^{-t/T_2}\Big(\cos(\omega_i t),\ \sin(\omega_i t),\ 0\Big). \tag{4.23}$$

Here, T_2 is the decay rate of the state, where $T_2 \ll T_1$. Thus, the effect of decoherence is a Bloch vector which shrinks towards the center of the sphere. The decoherence associated with the decay rate reflects a fundamental and irreversible loss of phase information to the environment. The end state is a classical mixture, where each level becomes equally populated.

The redistribution of the population between hyperfine levels is done by chaining $\pi/2$-pulses between them in sequence. This ensures that we do not trap the population in any of the levels. We therefore expect the levels to be sufficiently mixed after a number of repetitions of the pulse sequence N_{rep} have been applied. Here, N_{rep} represents the number of sequences where one sequence consists of four $\pi/2$-pulses that target $|\pm 1/2g\rangle \leftrightarrow |\pm 3/2g\rangle$ and $|\pm 3/2g\rangle \leftrightarrow |\pm 5/2g\rangle$ for each isotope.

A simple schematic showing the process on a TW is shown in Fig. 4.7. In essence, this is the scheme used to erase quantum information and obtain a classical state.

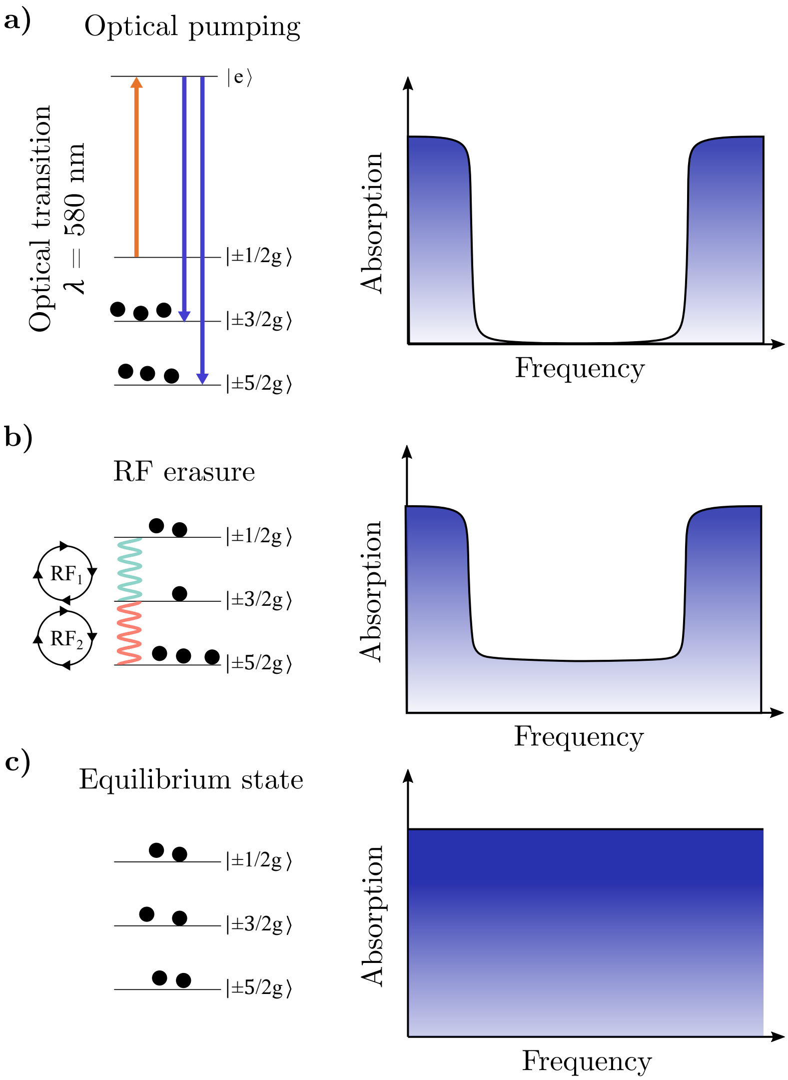

Figure 4.7: The method for erasure in a simplified four level system. In a), the ion population equilibrium is disturbed through optical pumping, moving ions to the $I = \pm 3/2$ and $\pm 5/2$ levels. Applying RF-field pulses to both transitions shuffles the population (b). The resulting end state is an equilibrium state (c) given appropriate pulse areas and repetition of pulses.

4.3.1 Pulse design

To coherently drive the ions from one state to the equator and ensure that all ions are affected the same, we need to have pulse durations such that $t_{\text{pulse}} < 1/\Gamma_{\text{s}}$, where Γ_{s} is the inhomogeneous spin broadening. The pulse area is given by $A = \Omega_0 t_{\text{pulse}}$ where the Rabi frequency is $\Omega_0 = \mu B_0/\hbar$, with μ as the magnetic dipole moment and B_0 the magnetic field. Thus, π-pulses generally require high magnetic fields, which may be difficult to achieve under certain circumstances. In our case, the input power to the circuit is limited by a voltage restriction on the switches ($< 100\,\text{V}$), resulting in a lower achievable B-field.

With limited power, one can instead use linear frequency-chirped pulses where ions can be excited coherently under adiabatic conditions.[69] This was discussed by Harris et al.[70] in the context of exciting optically dense inhomogeneously broadened media in Eu:YSO. They provided the fundamental relation between pulse chirp-rate and Rabi frequency for a two level system to achieve half-inversion (i.e, a $\pi/2$-pulse performed over a large bandwidth) given by the scaled dimensionless coupling strength:

$$\Phi = \frac{\Omega_0}{\sqrt{\Gamma_{\text{RF}}/\tau_{\text{RF}}}} \tag{4.24}$$

where Γ_{RF} the frequency scan range, and τ_{RF} the chirp duration. The ratio to prepare a half-inverted population, predicted by the Landau–Zener model, is $\Phi = 0.265$. In principle, one can measure the magnetic field and Rabi frequency and then change the chirp rate to achieve this ratio. However, as described in **Paper II**, we instead tuned the chirp rate to half-inversion pulses by preparing a known state and then running RF-pulses with different pulse durations. These states were read out optically through absorption measurements, where the desired end state (half-inversion) absorption footprint was simulated using a Bloch simulator. The parameter Φ then enabled us to connect the chirp rate to the effective magnetic field (and Rabi frequency) experienced by the ions. In order to target most of the ions with the chirped RF pulse, we decided to set the scan width Γ_{RF} to be approximately a multiple of the spin broadening Γ_{s}. As the spin broadening for the hyperfine transitions in natural-abundant europium at a doping concentration of 1 % was not known, this had to be measured first. These experiments have been described in the next section.

4.3.2 Spin broadening

To measure the inhomogeneous spin broadening, a 5 MHz wide spectral window was prepared. This was followed by narrow sech-scan pulses (scan width Γ_{peak}) performed at an offset frequency Δf_{tw}, relative to the center of the pit. The offset frequency Δf_{tw} would correspond to the center frequencies of the hyperfine splittings, depending on the transition being measured. Ions that are offset from the pit center by the hyperfine splitting can be optically addressed and transferred to the TW.

If the group of ions excited to the $^5D_0$ state is narrow (meaning Γ_{peak} is much smaller than the spin broadening Γ_{s}) then the ions that relax from $^5D_0$ will distribute according to the inherent inhomogeneous broadening of the spin transition. The burn-back width Γ_{s} was set to 50 kHz for most transitions. A wider window (5 MHz) was also chosen so that the edge absorption would not affect the spin broadened peak.

The result for the different transitions used in the RF pulse sequence is shown in Fig. 4.8. Inhomogeneous broadening was found to be greater for isotope 153 than for 151. The largest splitting was the $|\pm 3/2g\rangle \leftrightarrow |\pm 5/2g\rangle$ transition for isotope 153 around 119 MHz, which had a measured Γ_{s} of approximately 1.4 MHz. The smallest spin broadening was observed for isotope 151 at $|\pm 1/2g\rangle \leftrightarrow |\pm 3/2g\rangle$ with $\Gamma_{\text{s}} = 0.29\,\text{MHz}$. Fixing the necessary scan width to $3 \times \Gamma_s$ and using the pulse duration τ_{RF} required to achieve half-inversion for all the transitions used in the pulse sequence, we were ready to test the erasure performance of the tunable transmitter coil. As mentioned in the beginning of Section 4.3, the erasure experiments were performed on simple hole structures.

4.3.3 Ion decoherence during RF-pulses

So far we have assumed perfect coherence of the ions affected by the RF-pulses used to bring the ions from one hyperfine state to the equator of the Bloch sphere. To create a mixed state, a fully coherent pulse is preferred as this drives the Bloch vector more efficiently. In practice, however, these pulses are also limited by the spin coherence decoherence time $T_{2,s}$. To drive the state coherently, the time the RF field strongly interacts with any one ion should be short compared to $T_{2,\text{s}}$.

During a linear frequency sweep, the detuning $\Delta(t)$ changes linearly with time according to $\Delta(t) = \dot{\nu}t$, where $\dot{\nu}$ is the chirp rate. The ion interacts

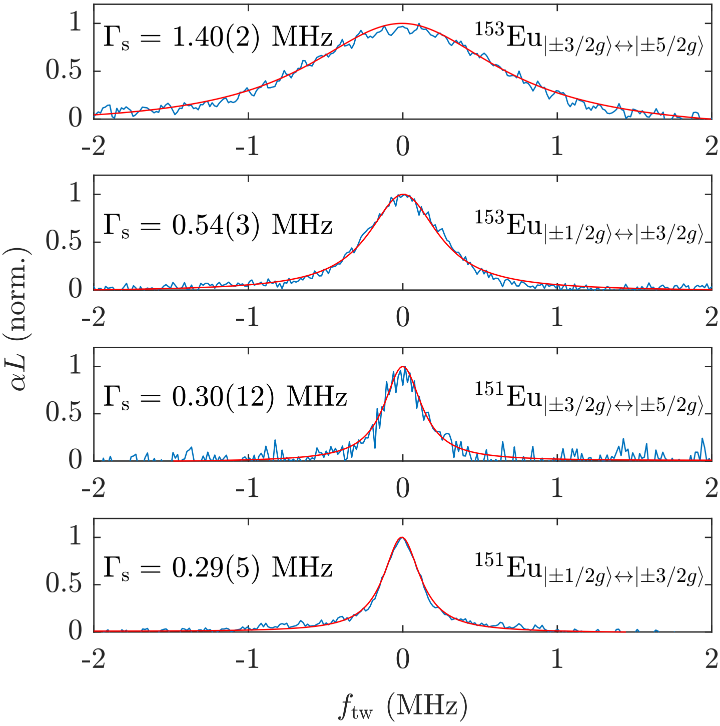

Figure 4.8: The inhomogeneous nuclear spin broadening Γ_s for adjacent transitions in Eu:YSO, including both isotopes.

most strongly with the drive near resonance, where the excitation probability is large. In the case of steady state excitation (with no decay), the excited-state population can be approximated as[33]:

$$\rho_{\mathrm{exc}}(\Delta) = \frac{\Omega_0^2/4}{\Omega_0^2/2 + \Delta^2}$$

which shows that the transition is most efficiently driven when the detuning Δ is small compared to the Rabi frequency Ω_0. In particular, when $\Delta = \sqrt{2}\Omega_0$, the excited-state population has already decreased to one-fifth of its maximum value. We will use this as a heuristic to define a natural frequency scale over which significant excitation occurs. We can then estimate the interaction time as the time it takes the sweep to traverse the frequency range $-\Delta$ to $+\Delta$ as:

$$t_{\mathrm{int}} \approx \frac{2\Delta}{\dot{\nu}} = \frac{2\sqrt{2}\Omega_0}{\dot{\nu}}.$$

This expression gives a simple estimate of how long the system is near enough to resonance to undergo coherent excitation. If this time is short compared to the coherence time $T_{2,s}$, the system can be expected to respond coherently during the sweep. The pulses used had interaction times t_{int} on the order of ms.

The chirp rate is $\dot{\nu} = \Gamma_{\text{RF}}/\tau_{\text{RF}}$ where $\Gamma_{\text{RF}} \approx 3 \times \Gamma_s$ to account for the broadening effects, and τ_{RF} is set to create a half-inversion state. From Eq. 4.24 we can then retrieve the Rabi frequency, which allows us to fully simulate the pulse dynamics using a Bloch simulator. Fig. 4.9 shows the ion transition path using the sweep parameters to create a half-inversion state for the $|\pm1/2g\rangle \leftrightarrow |\pm3/2g\rangle$ transition in isotope 151 with a calculated interaction time of $t_{\text{int}} \approx 0.8\,\text{ms}$, where $T_{2,s} = 15\,\text{ms}$.

The spin coherence has been measured in literature at a doping concentration of 0.1 %, without application of external static magnetic fields.[67,68] As no study of $T_{2,s}$ concentration dependence could be found, this value was used in the simulations. However, optical T_2 has been measured as a function of concentration, and no dependence was found up to a concentration of 1 %.[40]

4.3.4 Hole erasure

To demonstrate the efficiency of resetting the population in Eu:YSO, erasure was performed on 50 kHz wide holes. Initially, pulses were targeted on individual transitions to monitor the incremental response following each RF pulse. For full erasure, a sequence was created that systematically addressed all four transitions sequentially. The effectiveness of the erasure process was quantified by the absorption recovery degree, defined as the ratio $\alpha_{\text{e}}/\alpha_0$. Here, α_{e} represents the average absorption level within the TW after a pulse and α_0 the average absorption outside it. To maintain consistency, all absorption measurements used the same central frequency for the TW. For each transition, we sequentially applied five pulses, measuring the transmission after each individual pulse. Before applying RF pulses to target another transition, ions within the window were emptied through optical pumping. The results are illustrated in Fig. 4.10.

The application of multiple $\pi/2$-pulses on a specific transition is expected to drive the system toward equilibrium. A fully mixed level is then characterized by a recovery degree, which converges towards a particular value. In our system, this recovery degree settled around 30–32 %. How quickly the recovery degree converges depends on how well the pulse area matches an ideal $\pi/2$-pulse. As is evident from the experimental data, most tran-

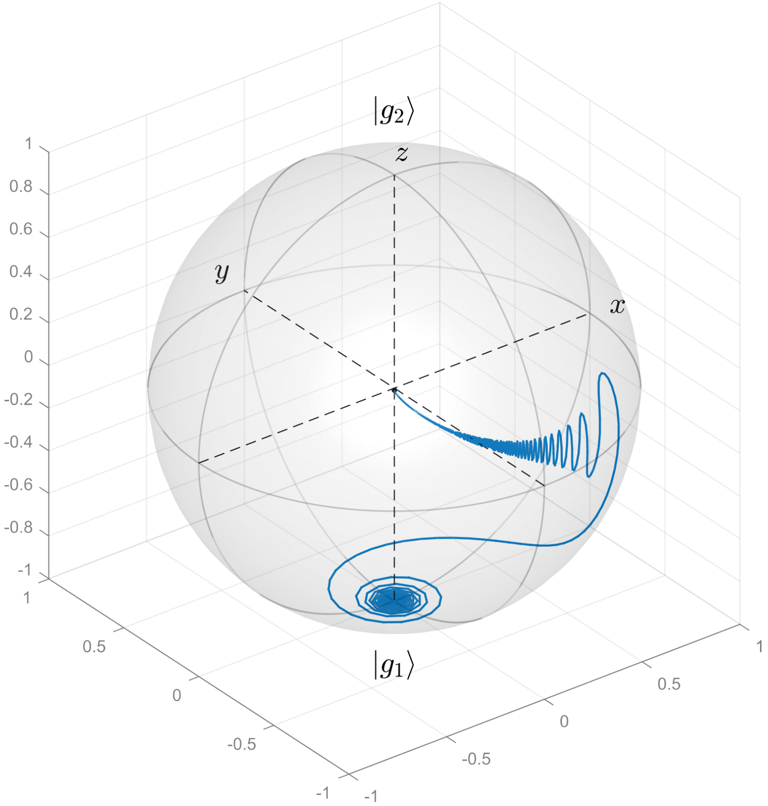

Figure 4.9: The Bloch vector state path for a single ion using the pulse parameters to drive the $|\pm 1/2g\rangle \leftrightarrow |\pm 3/2g\rangle$ transition. With a coherence time of $T_{2,s} = 15\,\mathrm{ms}$ the pulse can drive the ion to the equator plane where it is set to decohere, creating a mixed state. The transient simulated interaction time for the $\pi/2$-pulse from simulations was approximately $1\,\mathrm{ms}$.

sitions reach adequate mixing after only one or two pulses. However, the $^{153}\mathrm{Eu}_{|\pm 3/2g\rangle \leftrightarrow |\pm 5/2g\rangle}$ transition notably deviated from this behavior, failing to converge within five pulses. As the magnetic field generation efficiency for the transmitter coil was lower for higher frequencies and this transition had the highest spin broadening, it was difficult to achieve a pulse area close to $\pi/2$ in this case. Extrapolating the number of pulses required to fully mix this level resulted in about 15 pulses.

The black line shows the combined pulse sequence that includes all the transitions in one sequence. After five sequences the recovery degree approached 90 %, corresponding to an input energy of approximately 10 J.

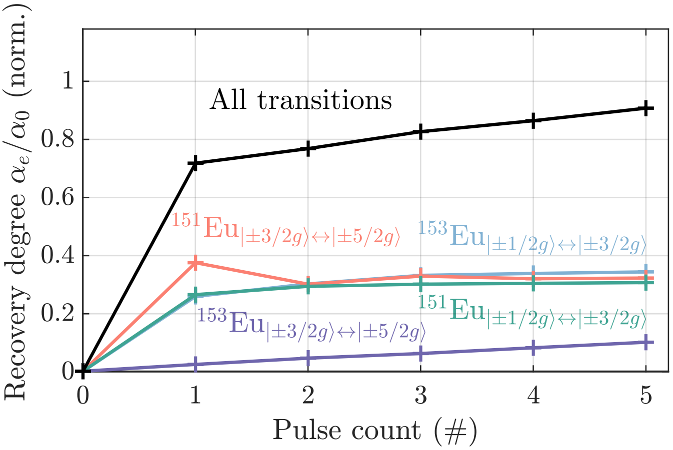

Figure 4.10: The erasure recovery degree (α_e/α_0) for each transition. Here α_e is the mean absorption inside the transmission window and α_0 is the absorption outside it. Each pulse was calibrated to have a pulse area as close to $\pi/2$ as possible. Given a transition, each pulse targeting it resulted in a recovery degree converging to a value of about 30–32 %. The blue and green curves correspond to slightly undertuned pulse areas, while the orange curve represents a pulse area $> \pi/2$. All transitions except for $^{153}\mathrm{Eu}\ |\pm3/2g\rangle \leftrightarrow |\pm5/2g\rangle$ could create a close to fully mixed state within 1–2 pulses. The black trace shows the combined pulse sequence targeting all transitions.

Adding more sequences beyond the first had little effect on the recovery degree, likely due to the smaller pulse area of the $^{153}\mathrm{Eu}_{|\pm3/2g\rangle\leftrightarrow|\pm5/2g\rangle}$ transition. Ideally, the combined recovery degree should reach unity for full recovery.

This erasure sequence was used in the slow light laser stabilization experiments to reset transmission windows after they have been degraded by the locking beam. During these experiments individual transitions were targeted five times each, apart from transition $^{153}\mathrm{Eu}_{|\pm3/2g\rangle\leftrightarrow|\pm5/2g\rangle}$ which was repeated 10 times.

Chapter 5

Laser stabilization using slow light

While Pound-Drever-Hall (PDH) locking provides increased frequency stability by locking the laser to a Fabry-Pérot cavity, the ultimate stability of such a system is constrained by the thermal and mechanical noise of the cavity. In particular, length fluctuations due to thermal noise in the mirror coatings impose a fundamental limit on the achievable frequency stability.[17,19,71] To overcome this limit, we take an alternative approach that takes advantage of the slow light effect within a highly dispersive optical medium.[72,73] The slow light effect arises from a sharp dispersion gradient in a medium, which significantly reduces the group velocity of light. In a cavity, this results in a longer group delay, making the light behave as if it were traversing a much longer effective path than the cavity's actual physical length. As a consequence, the frequency spacing of the cavity modes (free spectral range) is reduced, and the linewidths of the cavity resonances are significantly narrowed. The increased effective cavity length from the reduced group velocity improves frequency stabilization without the practical limitations of physically long cavities. Since fractional frequency sensitivity to length fluctuations decreases with increasing cavity length (see Ch. 2) the resulting frequency noise is lower. This allows frequency stability levels that would be difficult to achieve with conventional cavities at room temperature (see Eq. 2.3).

In **Paper III** we describe some properties of such a cavity doped with Eu:YSO, including frequency stability, matching conditions, and drift. This will also be the main focus in this chapter.

5.1 Highly dispersive materials

Highly dispersive materials are those in which the refractive index changes rapidly with frequency over a narrow spectral region. This steep dispersion can dramatically increase the group refractive index, leading to the so-called *slow light* effect, where the group velocity of light propagating through the medium is significantly reduced. High dispersion, as we will see, can be obtained from very narrow transmission windows in the inhomogeneous profile.

Electric susceptibility $\chi(\nu)$ describes how a material becomes polarized in response to an applied electric field at some given frequency. This susceptibility encodes both the real and imaginary parts of the medium response, where the real part χ' is associated with the refractive index and the imaginary part χ'' corresponds to absorption. The Kramers-Kronig relations mathematically express the link between the absorptive and dispersive components of a material's response, as required by the principle of causality. This connection arises from the basic physical principle of causality: a material cannot respond to an electromagnetic stimulus before the stimulus has been applied. It is given as[74]:

$$\chi'(\nu) = -\frac{2}{\pi}\mathcal{P}\int_0^\infty \frac{\nu'\chi''(\nu')}{\nu'^2-\nu^2}\mathrm{d}\nu' \tag{5.1}$$

Here, $\mathcal{P}$ denotes the Cauchy principal value of the integral. We can relate the absorption coefficent α to χ'' through

$$\chi'' = \frac{n_0\alpha}{k_0} \tag{5.2}$$

where k_0 is the vacuum wavenumber and n_0 is the refractive index for a weakly absorbing host. Once χ'' is known, $\chi'(\nu)$ can be retrieved via the Kramers-Kronig relation. The refractive index $n(\nu)$ is given by

$$n(\nu) = \sqrt{1+\chi'(\nu)} \tag{5.3}$$

for non-magnetic materials. The dispersion $\mathrm{d}n/\mathrm{d}\nu$ can then be directly calculated from this frequency-dependent refractive index. This formalism is particularly relevant in rare-earth-doped crystals such as Eu^{3+}:YSO, where narrow optical transitions can be used to create sharp features in both absorption and dispersion. The refractive index and absorption (normalized) have been plotted in Fig. 5.1 b) using Eq. 5.1 for a single europium ion with a measured absorption linewidth of Γ_h. The homogeneous linewidth Γ_h was obtained from the optical coherence time $T_{2,\mathrm{opt}}$ as

$$\Gamma_\mathrm{h} = \frac{1}{\pi T_{2,\mathrm{opt}}} \tag{5.4}$$

Before we continue to see why such a narrow linewidth allow us to obtain extremely high dispersion in Eu:YSO, I will just briefly mention the experiment done to measure the optical coherence time. The coherence time $T_{2,\mathrm{opt}}$ of the europium ions can be retrieved through optical echos, first introduced by Hahn in the context of spin echoes.[75] In this method, a coherent superposition of the ground and excited states is created using an optical $\pi/2$-pulse. Over time, the ions start to dephase because of inhomogeneous broadening in the local environment. After a delay τ, a refocusing π-pulse is applied, which inverts the phase evolution of the ions. This causes them to rephase and emit a photon echo at time 2τ. By varying τ and measuring the amplitude of the resulting echo, we can determine how coherence decays over time and extract the coherence time T_2. The result is shown in Fig. 5.1 a), where the decay time was measured to 0.748 ms, resulting in $\Gamma_\mathrm{h} = 426\,\mathrm{Hz}$. This is approximately 1.3 times broader than that measured by Könz[40], compared at an excitation density of $\rho = 18 \times 10^{12}\,\mathrm{cm}^{-3}$ and the same doping concentrations. Our experiments were carried out at a cell temperature of 1.3 K (MyCryoFirm) with 0.5 mbar helium in the cell to increase thermal conductivity. We also placed an additional temperature sensor (DT670-1.4 K, Lakeshore) mounted next to the crystal, which showed a reading of 3 K using a four-point measurement.

To investigate the discrepancy of the homogeneous linewidth, we can consider the contribution from instantaneous spectral diffusion Γ_ISD and temperature Γ_phonon separately (see Eq. 3.2), as derived by Könz.[40] Given a excitation density of $\rho \approx 18 \times 10^{12}\,\mathrm{cm}^{-3}$ this results in $\Gamma_\mathrm{ISD} \approx 16\,\mathrm{Hz}$. The phonon contribution at this temperature for site one was estimated down to 4 K for site 1, and here I extrapolate this contribution to 3 K, giving $\Gamma_\mathrm{phonon} \approx 16\,\mathrm{Hz}$ as well. The contributions from these models therefore do not explain the discrepancy alone.

Equall et al.[41] measured a linewidth of $\approx 200\,\mathrm{Hz}$ at the zero excitation density intercept at 1.4 K compared to $\approx 300\,\mathrm{Hz}$ at 2 K for Könz. This is a factor 1.5 broader in the case of Könz at a temperature delta of only 0.6 K. Thus, there may be some variance in a given sample from manufacturing. It should be noted that Equall had a doping concentration of 0.1 %. However, the homogeneous linewidth has also been found to be concentration independent.[40]

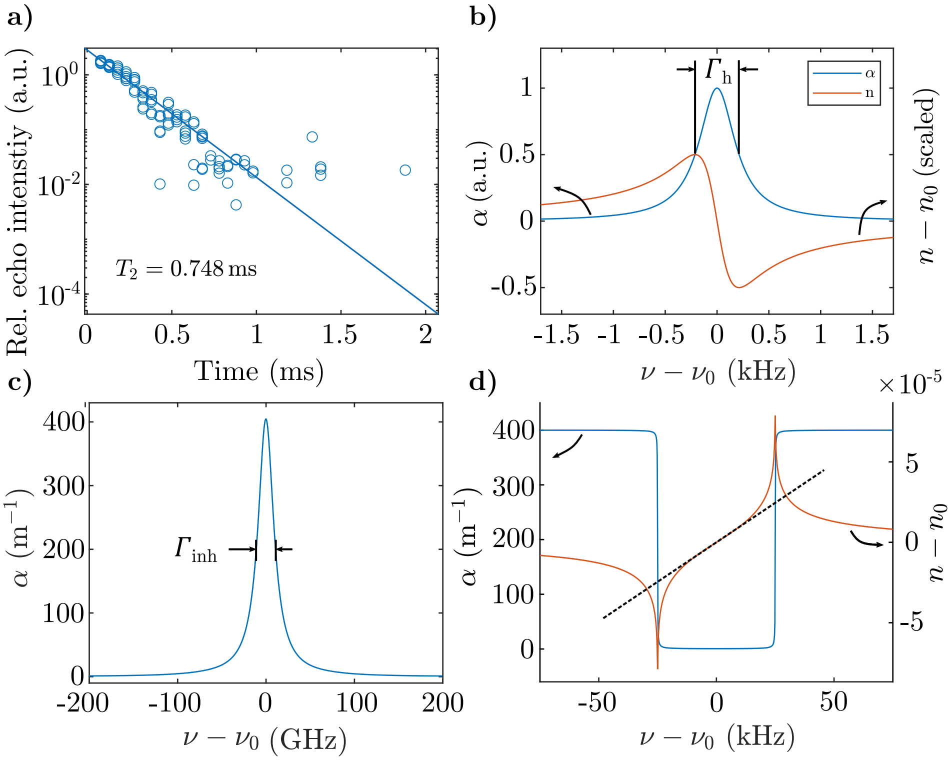

Figure 5.1: Eu:YSO as a highly dispersive medium. In a), the measured $T_{2,\mathrm{opt}}$ using echos, resulting in a homogeneous linewidth of the ion Γ_h shown in b) together with the ions Kramers-Kronig relation. The inhomogeneous broadening, fitted from measurements across the profile (c), and the large dispersion resulting from a narrow TW in d).

Continuing on the topic of dispersion and narrow homogeneous linewidths, it was explained in Ch. 3 that the resonance frequency of the individual ions will be shifted due to the slight variations in their crystal lattice environment. The resulting profile will be a convolution of all ions according to the distribution of the ensemble and the homogeneous linewidth Γ_h, leading to a homogeneously broadened linewidth of Γ_inh. In Fig. 5.1 c), a line fit of the absorption spectra of the measured broadened ion ensemble is shown. The line was fitted with a Lorentzian using several measurements spanning the profile. Due to the long hyperfine lifetimes and a very narrow homogeneous linewidth, ions can be optically pumped to create sharp transmission windows, as is theoretically illustrated in Fig. 5.1 d) for a 50 kHz window using the measured ion linewidth Γ_h. The TW is created at the peak of the inhomogeneous profile so that the dispersion effect can become large, with a group refractive index n_g approaching 5×10^5 in the center of the TW (see the following section for corresponding measurement). The group refractive index is defined as

$$n_{\mathrm{g}} = n_0 + \nu_0 \frac{\mathrm{d}n(\nu)}{\mathrm{d}\nu} \tag{5.5}$$

In the center of the TW the refractive index is approximately linear, with $\mathrm{d}n/\mathrm{d}\nu$ constant. The properties of the TW and how it relates to the refractive index can in this linear region be approximated by:[76]

$$n(\nu) = n_0 + \frac{2c\alpha}{\Gamma_{\mathrm{win}}\pi^2} \frac{\nu}{\nu_0} \tag{5.6}$$

where c is the speed of light, α the absorption, ν_0 the center frequency of the window, and Γ_{win} the window width.

5.1.1 Slow light

In most materials, light slows compared to its speed in vacuum because the oscillating electric field of the wave induces a response in the medium, delaying the propagation of each wavefront. This leads to a reduced phase velocity, which describes the speed at which individual crests and troughs move. However, a light pulse, used to transmit energy or information, is not a single wave but a superposition of a continuum of many closely spaced frequencies. The collective behavior of these frequency components determines the motion of the pulse envelope, which travels at the group velocity. Within dispersive mediums the different components of the pulse propagate at different speeds. This causes the pulse to broaden and move more slowly as a whole, resulting in the phenomenon of slow light. When sending pulses inside transmission windows where the refractive index changes rapidly with frequency, the slow light effect can become especially pronounced. The large dispersion in this case leads to group velocities which can be much lower than the vacuum light speed, c. The group velocity of a light pulse is given by,

$$v_g = \frac{c}{n_g} = \frac{c}{n_0 + \nu_0 \frac{\mathrm{d}n(\nu)}{\mathrm{d}\nu}} \tag{5.7}$$

A simple way to measure the group velocity is to send a pulse through a narrow TW and compare how long the delay is compared to a reference pulse. Figure 5.2 a) shows a window that was pumped very narrowly, having a window width of 30 kHz. A Gaussian pulse was sent through the center of the hole, traveling a distance of 21 mm (length of the crystal) while accumulating a delay of approximately $\Delta t = 35\,\mu$s. This corresponds to a group velocity of $v_g = 600\,\mathrm{m\,s^{-1}}$. We can of course compare this with the distance light would have traveled in vacuum, which is about 10.5 km. This illustrates how the group delay in the material effectively mimics the behavior of a much longer optical path.

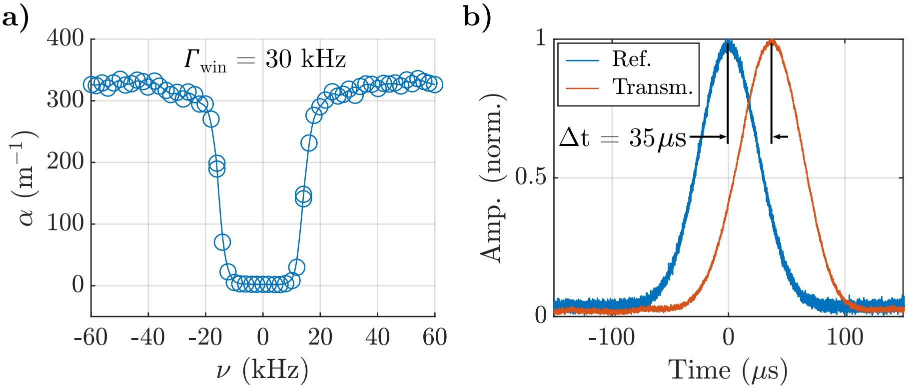

Figure 5.2: Pulse delay inside a TW. A narrow TW created through optical pumping using sechyp-pulses (left) and the resulting pulse delay obtained by sending a gaussian pulse through the center of it (right).

5.1.2 Fast light (Paper IV)

At first glance, the expression for group velocity seems straightforward, but its implications can be surprisingly counterintuitive. Notably, the sign of the group velocity can become negative under certain conditions, suggesting that a light pulse could exit a medium before it has fully entered.[77,78] This phenomenon, known as fast light, occurs in regions of anomalous dispersion where the refractive index decreases sharply with increasing frequency. As for slow light, this effect is also more pronounced near resonances. This was also the main idea behind **Paper IV** where efforts were made to spectrally tailor a specific absorption profile for which, when population inverted, result in sharp gain structures (negative absorption). The structure shares similarities with that of a TW, with the main difference being that the edges of the window are excited. The zero absorption region will then be located between two gain profiles on each side, where the dispersion factor becomes negative. Fig. 5.3 shows the result of a pulse arriving earlier in time compared to its reference, as is expected from a pulse with

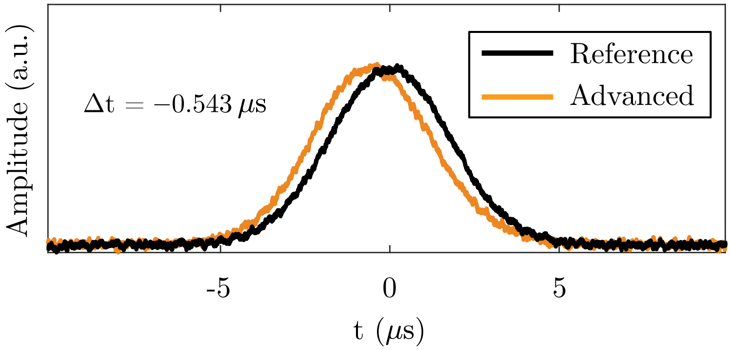

Figure 5.3: Pulse advancement from fast light, where the pulse seemingly exits the medium before it has fully entered it. The fast light pulse (yellow) was timed to arrive $-0.54\,\mu\mathrm{s}$ before the reference pulse (black).

negative group velocity. In these regimes, the frequency components of the pulse interfere in a way that reshapes the pulse envelope and shifts its peak forward in time. While this can result in group velocities exceeding the speed of light in vacuum (or even becoming negative), it does not violate causality. No new information can be obtained from the leading edge of the fast light pulse, as this information is already encoded in the tail ends of it. Fast light is thus a manifestation of pulse reshaping through coherent interference, not a breach of relativistic limits. Thus, information still remains bounded by the speed of light.[79]

5.2 Eu:YSO as a slow light plane-parallel mirror cavity (Paper III)

The cavity sample consisted of a single crystalline yttrium orthosilicate (Y_2SiO_5, YSO) grown by *Scientific Materials*. The crystal was doped with europium ions (Eu^{3+}) at a concentration of 1 atomic percent (that is, 1 % of yttrium ions have been replaced with Eu^{3+}), using europium in its natural isotopic composition. This results in nearly equal populations of the two stable isotopes, ^{151}Eu and ^{153}Eu, both of which possess nuclear spin $I = \frac{5}{2}$.[35] In the host lattice, the dominant isotope ^{89}Y has a nuclear spin of $I = 1/2$ and a very small magnetic moment. The other lattice constituents contribute minimal additional magnetic noise. Silicon ^{29}Si, has a natural abundance of only 4.7 % and nuclear spin $I = 1/2$. Magnetic oxygen isotopes have very little magnetic interactions due to the negligible abundance of just 0.04 %.[40] These characteristics make YSO a favorable host for reducing magnetic noise and achieving a narrow linewidth.

YSO crystallizes in the monoclinic system with space group C2/c, containing two inequivalent crystallographic sites for yttrium. Europium ions (Eu^{3+}) replace Y^{3+} in these sites without significantly disturbing the host lattice due to the similarity in charge and ionic radius (although still large enough to see inhomogeneous broadening). Both of these substitution sites have local site symmetry C_1, that is, they do not have symmetry elements. The crystal was cut along the optical axes with dimensions 14 mm × 15 mm × 21 mm, corresponding to $b \times D_1 \times D_2$. This is shown in Fig. 5.4 a). For a 1 % doping concentration, the maximum absorption along these axes is $\alpha_b \approx 0$, $\alpha_{D_1} = 390\,\mathrm{m}^{-1}$, and $\alpha_{D_2} = 80\,\mathrm{m}^{-1}$[40]. The important polarization for locking is D_1, as this maximizes the dispersion of our linearly polarized beam.

To make a cavity out of the crystal, mirrors with reflectivities of $R_1 = 90\,\%$ and $R_2 = 99\,\%$ were deposited on the faces by *Optoman* using ion beam sputtering. The mirror coatings consisted of a SiO_2/Ta_2O_5 amorphous dielectric stack. A corner was left uncoated to enable absorption measurements. However, before depositing the mirrors the crystal faces had to be polished. To avoid the broadening effects of the mode, it is important to consider the parallelism and surface roughness of the reflective faces. Any wedge angle between the mirrors can reduce the coupling efficiency and degrade the linewidth. Surface roughness, typically quantified as an RMS deviation from flatness over a specified area, affects scattering losses within the cavity. Thus, minimizing both the angle of the wedge and the roughness of the surface is important to achieve well-defined interference conditions.

The crystal was first mechanically polished by *Edmund Optics* to minimize the wedge angle between the mirror faces to about 8 µrad. This prepolish was a necessary step before a superpolish could be performed by *Neue Technologien* using ion beam forming, resulting in a surface flatness of 1 nm RMS over a 1 mm diameter (see Fig. 5.4 b) and a wedge angle of 1.37 µrad. During the polishing process, spatial inhomogeneities in the crystal refractive index were identified. It was not possible to make both cavity surfaces flat while also achieving optical flatness through the material. Therefore, one side was chosen to be physically flat while the other side was used to compensate for refractive index inhomogeneities to make it *optically* flat. This ensured that the cavity behaved as flat from an optical point of view, which is the important part in this case. The measured relative length values across the crystal face in Fig. 5.4 c) refers to this flatness.

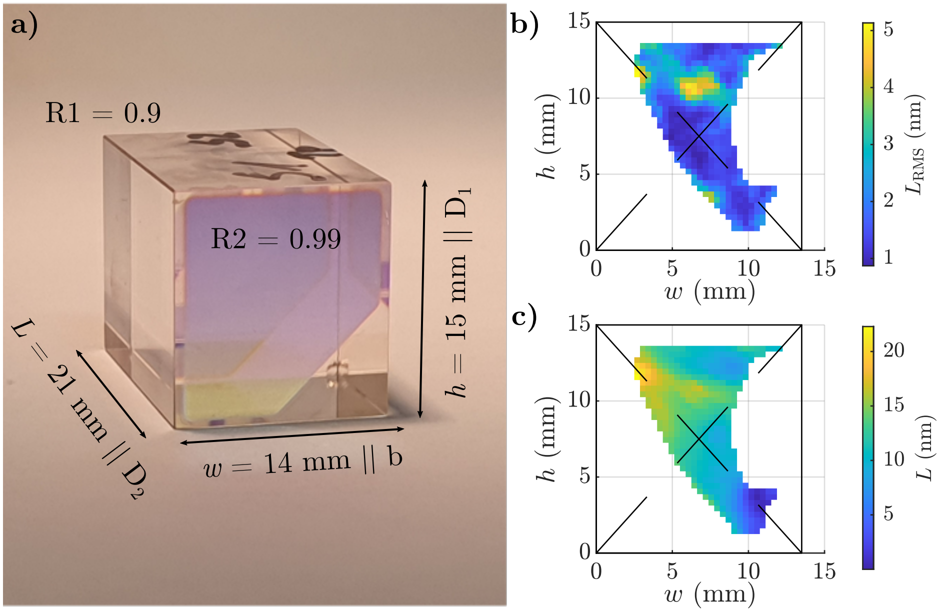

Figure 5.4: The mirror coated and polished Eu:YSO crystal used in the experiments. The crystal with length dimensions and polarization axes labeled (a). The corresponding surface roughness (b) and relative length across the cavity (c) from the perspective of the mirror with a reflectance of R1.

5.2.1 Cavity impedance matching

Following the derivation by Siegman[80] the reflected field of a cavity $\tilde{E}_{\text{ref}}$ will consist of a component $r_1\tilde{E}_{\text{inc}}$ due to the direct initial reflection off the mirror M_1, plus a second component which represents the circulating field $\tilde{E}_{\text{circ}}$ inside the cavity. This second component comes from light that has circulated the cavity and then been transmitted through the input mirror. The resulting field of this component is $it_1(\tilde{g}_{\text{rt}}/r_1) \times \tilde{E}_{\text{circ}}$. We can then write

$$\tilde{E}_{\text{ref}} = r_1\tilde{E}_{\text{inc}} + it_1(\tilde{g}_{\text{rt}}/r_1) \times \tilde{E}_{\text{circ}} \tag{5.8}$$

where $\tilde{g}_{\text{rt}}$ is the complex round trip gain. The magnitude of this round-trip gain will of course be less than unity $|\tilde{g}_{\text{rt}}| < 1$ in any passive optical cavity due to losses present.

With knowledge of the reflected field, we obtain the reflection ratio $R_{\text{cav}} = I_{\text{ref}}/I_{\text{inc}} = (\tilde{E}_{\text{ref}}/\tilde{E}_{\text{inc}})^2$ which describes the power reflectivity of the cavity.

The reflected power of a cavity can then be expressed as:

$$R_{\mathrm{cav}} = \left| \frac{1}{\sqrt{R_1}} \frac{R_1 - \tilde{g}_{\mathrm{rt}}}{1 - \tilde{g}_{\mathrm{rt}}} \right|^2 \tag{5.9}$$

where R_1 is the reflectivity of the input mirror. When the cavity is critically coupled, the input mirror reflectivity R_1 will be equal to the round-trip gain $\tilde{g}_{\mathrm{rt}}$. This condition is known as impedance matching, where the cavity is designed to minimize reflections. The round trip gain is,

$$\tilde{g}_{\mathrm{rt}} = \sqrt{R_1}\sqrt{R_2} e^{-\alpha/2L_{\mathrm{rt}}} e^{-i\phi} \tag{5.10}$$

and includes the reflectivity of the output mirror R_2, the round trip absorption α, and the round trip phase ϕ. The term $e^{-\alpha/2L_{\mathrm{rt}}}$ represents an amplitude reduction of the light due to medium absorption and scattering losses. The round trip phase ϕ describes the phase shift accumulated by the light during one round trip in the cavity. As mentioned, impedance matching means $\tilde{g}_{\mathrm{rt}} = R_1$ which implies the following conditions needs to be satisfied:

$$\begin{aligned} R_1 &= R_2 e^{-\alpha L_{\mathrm{rt}}} e^{-i2\phi} && (5.11) \\ \mathrm{Re} : \alpha L_{\mathrm{rt}} &= \ln\left(\frac{R_2}{R_1}\right) && (5.12) \\ \mathrm{Im} : \phi &= 2\pi n, \quad \text{where } n \in \mathbb{Z}. && (5.13) \end{aligned}$$

When on resonance ($\phi = 0$), we can see from Eq. 5.11 that it is the product between $R_2 e^{-\alpha L_{\mathrm{rt}}}$ that matters for matching and it does not matter to the total reflectivity at mirror M_1 how the rest of the cavity losses are divided between the second mirror M_2 and the internal losses $e^{-\alpha L_{\mathrm{rt}}}$.

This cavity was designed to impedance match the cavity by tuning the round-trip internal losses (absorption losses), α. Optically pumping ions will excite a majority of ions and move them to another ground state, leaving a transparent region in the absorption profile. However, after burning a TW there will always be ions close to the edges of the pit that have the chance to absorb because of their homogeneous linewidth, Γ_{h}, extending into the pit. In the center of the pit, the theoretical remaining absorption for a transmission window with a square ion distribution is given by

$$\alpha_{\mathrm{c}} = \frac{2}{\pi} \cdot \frac{\Gamma_{\mathrm{h}}}{\Gamma_{\mathrm{win}}} \cdot \alpha_{\mathrm{edge}} \tag{5.14}$$

where Γ_{win} is the window width, and α_{edge} the edge absorption. Naturally, residual absorption in the center of the window can be offset by making the window wider, as this reduces the probability of absorbing ions close to the edge. This approach for matching was investigated in **Paper III**. In Fig. 5.5 a) impedance matching is demonstrated by burning transmission windows with different pit widths at 1.5 K. A minimum in R_{cav} can be observed around $\alpha_{\text{c}} L_{\text{rt}} = 0.09$, equivalent to a hole width of approximately 50 kHz.

Although a minimum in reflectivity could be located, it was not possible to obtain perfect mode matching where $R_{\text{cav}} \approx 0$. A fit (on resonance) was applied using Eq. 5.9 and 5.10 together with a non-coupling factor R_{nc}. This factor represents the portion of light that is immediately reflected as a result of a spatial mode mismatch. The absorption was set to $\alpha = \alpha_c + \alpha_{\text{rem}}$, where α_{rem} represented the remaining intracavity losses. Both α_{rem} and R_{nc} were used as fit parameters, resulting in $R_{\text{nc}} = 37\,\%$ and $\alpha_{\text{rem}} = 0.0038$. From this experiment, we concluded that cavity reflectivity increases with window width for the widest transmission windows. This means that the losses in the cavity are low enough to achieve impedance matching for narrower windows (which have higher absorption losses from α_c).

We suspect that the readout of the narrowest modes may have been limited in resolution, which could explain the lower measured mode matching. As the mode width decreases from narrowing the TW, a broadband laser will not be able to resolve the mode properly. Thus, this can lead to a readout which appears to have a larger proportion of non-coupled light. To investigate this further, mode matching was also performed across the absorption profile at room temperature, where the modes are wide enough not to be limited by the resolution of the readout. In Fig. 5.5 b), it is shown how the inhomogeneous absorption profile can be used to match the cavity. The absorption profile follows a Lorentzian distribution that extends several hundreds of GHz. This creates a naturally varying absorption profile that can be used to impedance match the cavity. The absorption profile was estimated from the inhomogeneous profile at cryogenic temperature under the assumption that the area is preserved as the linewidth increases from a change in temperature. A few reflectivity measurements were taken across a wide frequency range. Starting at the frequency farthest away from the peak, the mode was first matched to best effort to the cavity. At this frequency, the reflected light from the cavity was about 5 %. Closer to the peak, the reflectivity increases as a result of the increase in absorption. In general, this experiment shows that the cavity can couple well.

However, no impedance matching minimum was observed here because the absorption profile is very wide reaching at room temperature. At cold tem-

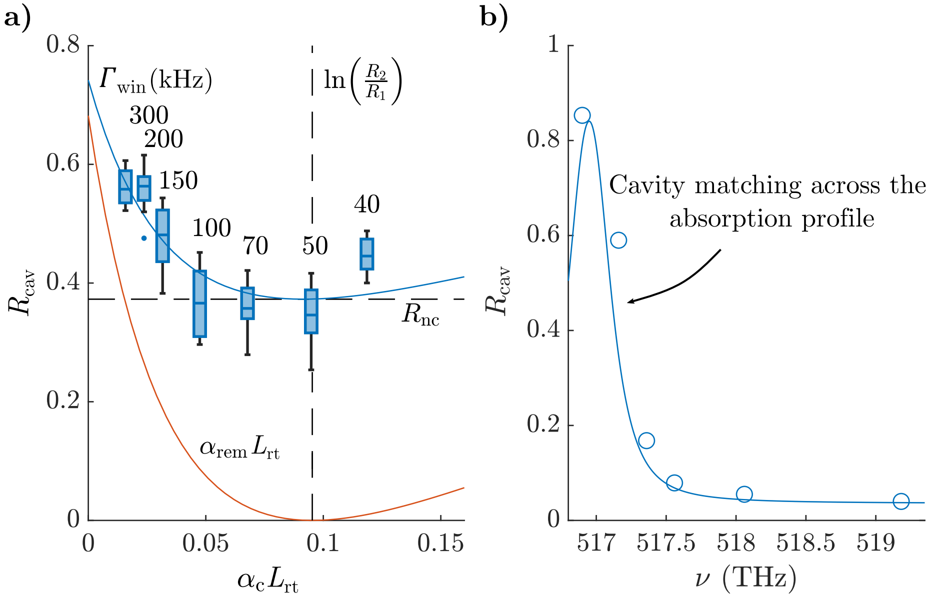

Figure 5.5: Impedance matching of the cavity. In a), impedance matching inside a transmission window via window size tuning. The optimum window size was approximately 50 kHz. The cavity reflection sampled at a few points along the absorption profile at room temperature (b). The matching becomes better as the losses decrease from absorption.

peratures, the cavity has an inhomogeneous linewidth of about 10 to 15 GHz at a doping concentration of 1 %. At room temperature, the line shifts and broadens significantly.[40] The line fit, based on linewidth and inter-cavity round-trip losses as fitting parameters, gave a linewidth of approximately 143 GHz and losses of about 5 %. R_{nc} is expected to be lower than or equal to the minimum reflectivity measured and was set to 3 %. The extra losses may be attributed to broadened and shifted distant satellite absorption peaks, measured by Sellars et al.[81] at cryogenic temperatures. However, these peaks were only measured up to a frequency offset of approximately 0.5 THz.

5.3 Locking to a high Q slow light cavity (Paper III & V)

The slow light effect in a dispersive cavity fundamentally alters the cavity response to length fluctuations by reducing the group velocity of light.

This reduction not only enhances the effective cavity length but also leads to a narrowing of the mode cavity linewidth, directly improving frequency stability. When a medium with a strong dispersion profile is introduced into the cavity, the group velocity v_g becomes significantly reduced, modifying the free spectral range (FSR) as

$$\nu_{\mathrm{FSR}} = \frac{v_g}{2L} \tag{5.15}$$

Since the linewidth of a cavity mode is given as $\Delta\nu_{\mathrm{cav}} = \nu_{\mathrm{FSR}}/\mathcal{F}$, it can also be written:

$$\Delta\nu_{\mathrm{cav}} = \frac{v_g}{2L\mathcal{F}} \tag{5.16}$$

Thus, a lower group velocity leads to a proportionally narrower cavity linewidth of the mode. In **Paper III** we demonstrated a transmission linewidth of approximately 3 kHz resulting in a Q-factor of 1.7×10^{11}. The measured relative frequency stability (which will be discussed further in Section 5.3.2) was, however, limited by fiber noise.

Fiber noise can be considered technical noise and is not fundamentally limiting to slow light laser stabilization. However, even though technical noise such as temperature fluctuations, mechanical vibrations, and electrical noise are not fundamentally limiting, it still requires much time and resources to reduce. As we are mainly concerned about reducing fundamental noise like Brownian motion induced frequency noise, it would be preferable to benchmark how slow light cavities perform in this regard. In **Paper V** we present a method for isolating Brownian motion-induced frequency noise using dual-beam interrogation of the cavity. As most technical noise can be considered common mode, it can be rejected by comparing both beam paths. Thus, this approach allows us to ignore these noise sources to some extent.

However, before diving into more detail, I will take a moment to describe the experimental setup used for the dual beam experiments, as presented in Fig. 5.6. This setup resembles, for the most part, a standard PDH locking loop. A rhodamine 6G dye laser (Coherent, 699-21) was pre-stabilized by locking it to an ULE cavity with a construction similar to that described in ref.[82] An AOM in double pass (1.5 GHz) was used to shift the frequency between the laser and the ULE cavity. The free space beam was coupled to a 10 m long fiber and brought to another optical table where the experiments were carried out. The beams were split into two beam paths with the intention of having two independent PDH locking loops for the same cavity. The feedback system consisted of an AOM (Isomet, M1201-

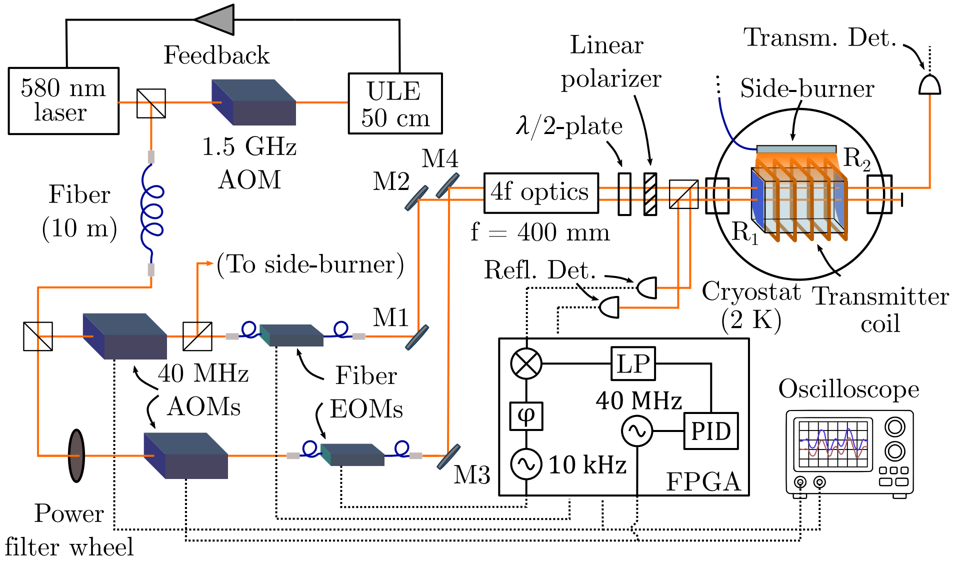

Figure 5.6: The experimental setup using dual beams and locking loops. With identical locking loops, the beams impinge on spatially different spots on the crystal. The beam positions are adjusted using individual aligntment mirrors (M1-M4) and a common $4f$ setup where both beams can be translated simultaneously. The locking loop is controlled by a FPGA digitally (only one path shown). The control signal for both traces is recorded on an oscilloscope. Black traces are digital signals while dashed are analogue.

SF40) operating at 40 MHz, a fiber-coupled EOM (Jenoptik, PM594) for sideband generation, high-stability mirrors for independent beam alignment on the crystal (Thorlabs, Polaris), and a low-noise transimpedance amplifier (NF corp, SA-606F2) with a photodiode connected (Hamamatsu, S5973-02) to measure the reflected light from the cavity. The detected signal was first high-pass filtered at 3 kHz to remove low-frequency noise (not shown in the figure) before being digitized by an analog-to-digital converter (ADC) on a field-programmable gate array (FPGA) (Koheron, alpha-250). The FPGA processed the signal through demodulation by making a phase comparison between the 10 kHz EOM modulation and the reflected light, extracting the PDH error signal. This error signal was then passed to a proportional-integral-derivative (PID) controller, which calculated the necessary frequency correction to maintain laser lock.

The correction signal from the PID controller was sent to a numerically controlled oscillator (NCO), which generated the 40 MHz RF signal used to drive the AOM. The NCO dynamically adjusts the AOM drive frequency

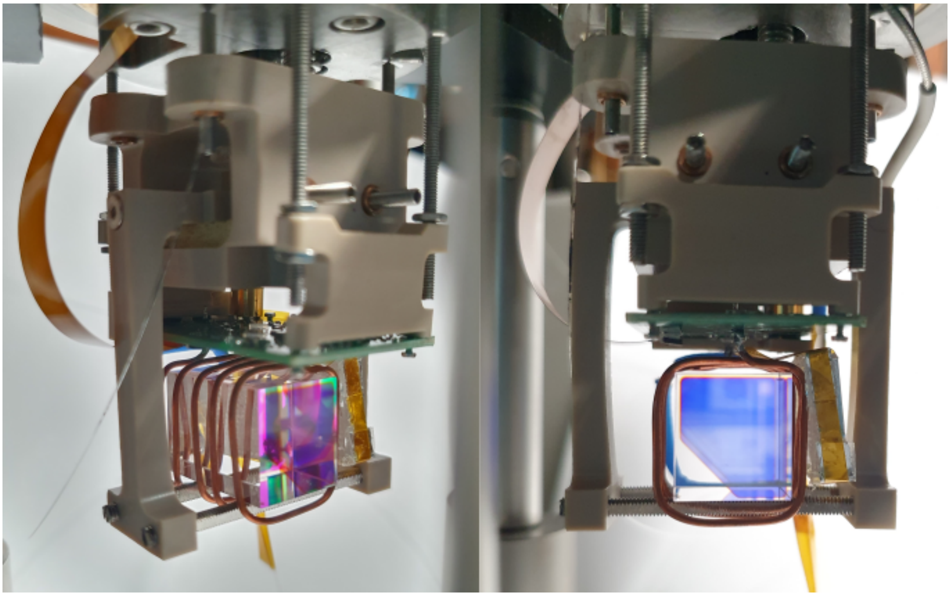

Figure 5.7: The holder used to mount the crystal. The crystal is laying on two cylindrical rods attached to U-shaped bracket which is resting on Kapton foam to isolate it from vibrations. The main structure have been spring-loaded to the cell lid. Visible is also the transmission coil with circuitry, and the sideburner (attached on the right side in the right view)

in response to the PID output, shifting the laser frequency to compensate for deviations from cavity resonance. Finally, the modulated RF signal is converted to an analog output via a digital-to-analog converter (DAC) and routed to the AOM.

Although the locking loops are identical component-wise, the two beams are spatially separated on the crystal and probe different sets of ions. This setup effectively creates two independent cavities. By comparing the stabilized laser frequencies associated with each beam spot, we can isolate the thermal noise contribution from uncorrelated atomic motion at different positions on the cavity mirrors. This was the primary interest of this thesis and the experiments have been detailed in Section 5.3.2.

5.3.1 Frequency sensitivity

The lock frequency sensitivity is determined by the slope of the error signal at the lock point, which quantifies how small frequency deviations translate into measurable voltage changes. This slope, known as the frequency discriminant, is inversely proportional to the linewidth of the cavity. A large frequency discriminant improves the lock's ability to reject frequency noise and track small detunings. It is defined as[15]

$$D = \left| \frac{\mathrm{d}V_{\mathrm{err}}}{\mathrm{d}\nu} \right| \tag{5.17}$$

where V_{err} is the measured error signal voltage. In the vicinity of the zero crossing the error signal can be approximated as a straight line with an inclination determined by the PDH discrimination slope which is proportional to the cavity line-width as

$$D \propto \frac{1}{\Delta\nu_{\mathrm{cav}}} \tag{5.18}$$

Thus, as the mode linewidth narrows due to slow light, the slope of the error signal steepens. Figure 5.8 presents the transmission mode, reflection mode and error signal for the cavity inside a 50 kHz hole using a 10 kHz modulation frequency. The mode width obtained after dispersive enhancement was approximately 3 kHz for the transmission mode and around 1.5 kHz in reflection, resulting in a frequency discriminant of $0.04\,\mathrm{V\,kHz^{-1}}$ with 1 nW on the reflection detector.

5.3.2 Short-term frequency stability

Short-term frequency stability is commonly quantified using a metric called Allan deviation[83,84], which characterizes the statistical variation of frequency over different time scales. A perhaps more intuitive explanation for the Allan deviation is that we evaluate the stability of a clock by starting and stopping it over various time intervals (τ). By doing this, we can examine the variations in the clock's frequency over these successive periods. At short averaging times, the Allan deviation is typically higher because high-frequency noise and rapid fluctuations dominate frequency variations over short intervals. As the averaging time increases, fast variations are averaged, revealing the underlying stability of the system. The frequency stability typically improves until gradual drift can be seen, caused

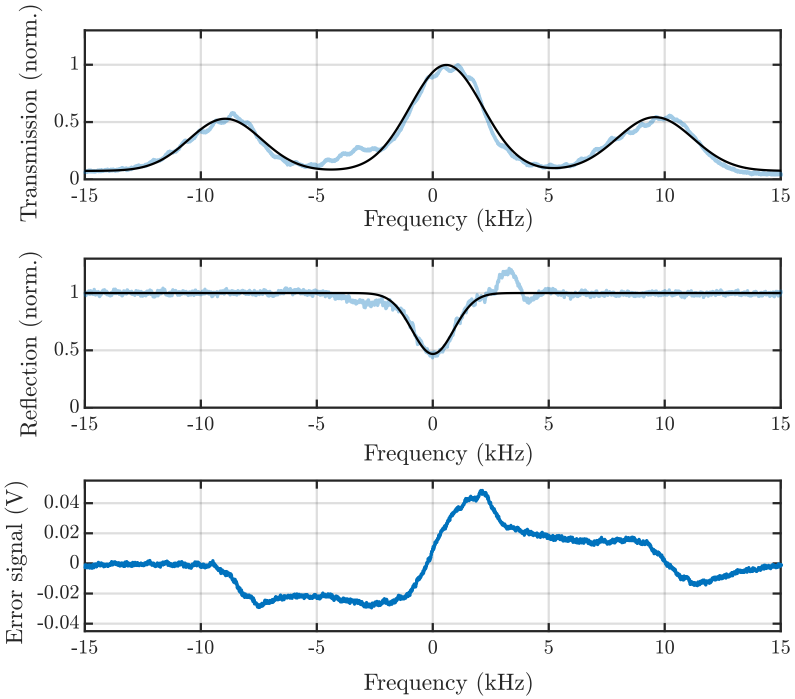

Figure 5.8: Transmission and reflection modes read out while phase modulating the light at 10 kHz using an EOM. The modulation depth used $\beta \approx 1.08$ resulted in sidebands with an amplitude slightly larger than half the amplitude of the carrier. The error signal shows the asymmetric response around resonance.

by slow systematic changes in frequency over time. Thus, the Allan deviation helps identify and quantify these different types of instabilities affecting the clock's performance over short and long durations. The Allan deviation can be measured from a time series data set as[84],

$$y(t) = \frac{\nu(t) - \nu_0}{\nu_0} \tag{5.19}$$

where the Allan deviation is defined as,

$$\sigma_y(\tau) = \sqrt{\frac{1}{2}\left\langle \left(\bar{y}_{i+1} - \bar{y}_i\right)^2 \right\rangle} \tag{5.20}$$

Here $\langle\ \rangle$ denotes the expectation value (average) and $\bar{y}_i$ is the ith sample of the average of y over some observation time τ. To increase statistical confidence, it is common to use an overlapping Allan deviation. In this case, each τ bin has data points that count toward several other bins.[84] This is also how the Allan deviation was calculated in this thesis.

Since any noise in the error signal is indistinguishable from true laser frequency fluctuations, the ultimate limit to frequency stability is set by quantum shot noise.[15] This defines the shot-noise-limited Allan deviation, representing the lowest achievable noise floor. The Allan deviation in this limit is related to the frequency noise associated with the spectral density of the shot noise S_e. The corresponding frequency noise is given by $S_f = S_e/|D|$, where D is the frequency discriminant. Following the derivation of Black[15] and using the frequency ν_0 to normalize the expression to be consistent with Riley[84], it is given by

$$\sigma_y(\tau) = \frac{1}{\sqrt{2\tau}} \frac{1}{4} \sqrt{\frac{h\nu_0}{P_\mathrm{c}} \frac{\Delta\nu_\mathrm{cav}}{\nu_0}} \tag{5.21}$$

where P_c is the carrier power of the locking beam and h Planck's constant. Using realistic values for our cavity with $\tau = 1\,\mathrm{s}$, $\nu_0 = 517 \times 10^{12}$ Hz, $P_\mathrm{c} = 1\,\mathrm{nW}$, and $\Delta\nu_\mathrm{cav} = 1.5\,\mathrm{kHz}$, this would result in an Allan deviation of approximately 1×10^{-17}.

The instantaneous frequency shift, $\nu(t)$, can be measured in a PDH locking loop by recording the PID feedback signal passed to the AOM responsible for shifting the frequency of the mode back on resonance. The idea here is to use dual beam interrogation of the cavity, where most technical noise is assumed to affect both beam paths in the same way so that it is correlated. This will be referred to as common mode noise, which can be considered correlated. By comparing the two beam paths, this shared noise can be largely rejected, allowing the differential signal to highlight uncorrelated effects. If the lateral beam positions on the mirrors are well separated, this should result in uncorrelated noise from the atoms being probed, so that the instantaneous differential frequency $\Delta\nu_\mathrm{diff}(t) = \nu(t)_\mathrm{out,1} - \nu(t)_\mathrm{out,2}$ can be dominated by Brownian noise. However, it should be noted that any common mode noise that is canceled (like fiber noise, mechanical noise, etc.) still contributes to the noise level of the laser. There is no gain in this dual beam approach in reaching an absolute frequency stability beyond these noise levels without implementing proper noise reduction techniques for this type of technical noise.

In Fig. 5.9 a) the instantaneous frequency feedback signals $\nu(t)_\mathrm{out}$ for both AOM's have been recorded and overlapped in time. The resulting differential frequency $\Delta\nu_\mathrm{diff}(t)$ is also shown. As shown in the inset plot, most of the noise is correlated, which can be canceled by subtracting the signals. The Allan deviation for the dual beam $\Delta\nu_{\mathrm{diff}}(t)$ is shown in Fig. 5.9 b). Single beam traces (**Paper III**) at different locking powers have also been included as reference. The dual beam lock was able to reach an Allan deviation of 9×10^{-15} for $\tau \approx 0.15\,\mathrm{s}$. The lowest noise level for the single beam approach (6×10^{-14}) could be reached within three orders of magnitude lower τ. For longer averaging periods, the level of noise approached 1×10^{-14} before onset of drift became apparent. The early onset of drift compared to the single-beam locks is likely due to relative mode drift between the two modes. The drift experienced by each mode depends on the relative position within the window. Thus, if the modes are separated in frequency, they will have different drift rates, which can be problematic. This will be discussed in more detail in the following section, where I will touch on some of the drift-related concepts when locking with both single and dual beams, including some considerations made during the experiments. As there is no clear noise plateau in the case of dual beams (see for example Nicholson[85]), this suggests the stability was mainly limited by drift. Since each loop used a separate fiber-coupled EOM with approximately 1 m of fiber, the fiber length may have been too long to avoid drift from environmental factors such as thermal fluctuations. Using a common EOM would have ensured that such variations were common-mode and could be canceled when comparing the frequency of both beams.

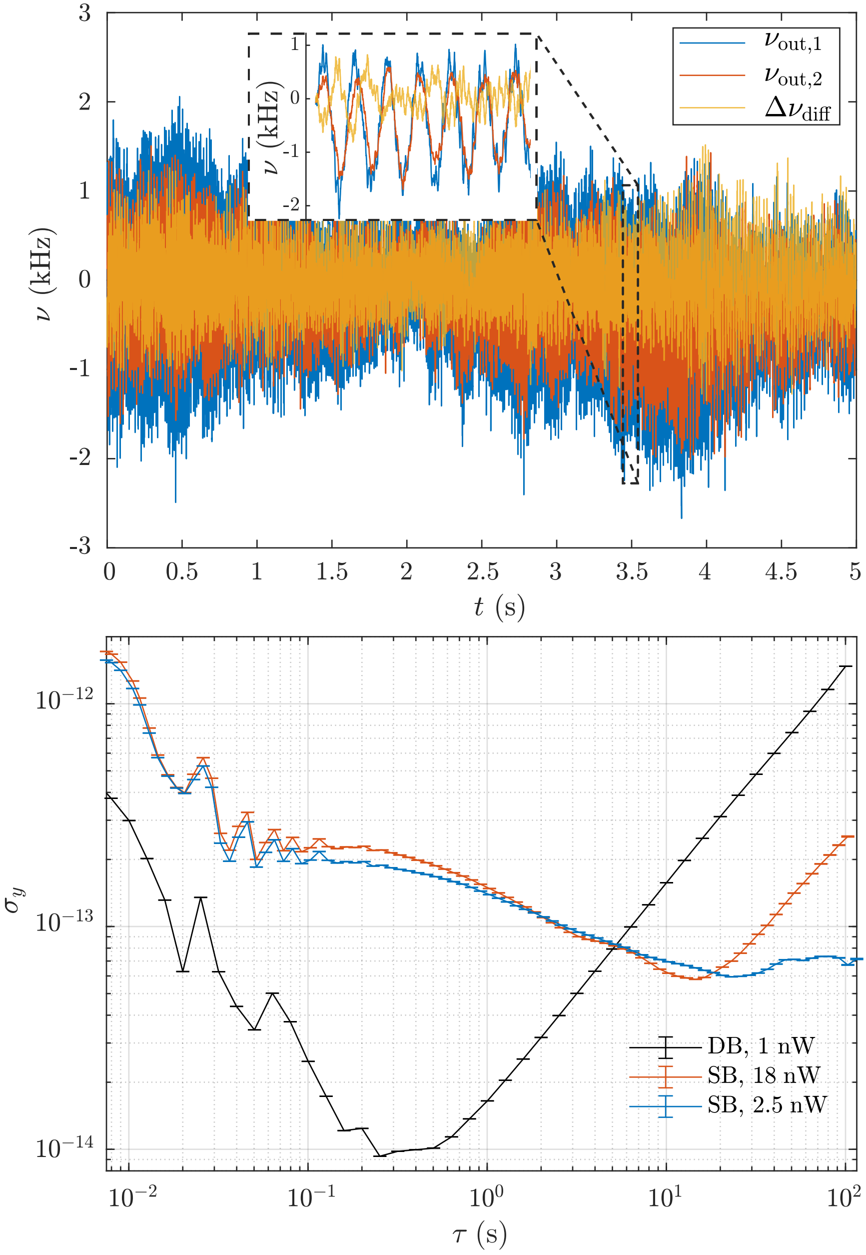

Figure 5.9: The frequency control signal for each locking loop and the resulting differential frequency (top). Allan deviation calculated for the differential trace and single loop traces with different locking powers (bot). The TW width Γ_{win} used was $50\,\mathrm{kHz}$ and the relative distance between the modes in frequency was $\sim 1\,\mathrm{kHz}$. Linear drift is subtracted.

5.3.3 Drift

Depending on the position of the mode inside the TW (in relation to the center) and the locking power used, the mode will experience different drift rates during locking. As was shown by Horvath et al.[50], the closer the mode is to the edge of the window, the higher the drift will be. The cause of this is mainly attributed to off-resonant excitation, where asymmetric burning of the edges of the window from the locking beam results in the mode drifting. Thus, just as for single beam locking, it is beneficial to move the modes to a low drift-rate position at, or close to, the center of the window. The best-case scenario here, of course, is to have both modes centered and overlapped.

Before discussing how one could achieve this, I would like to start by explaining how the position of the TW in the inhomogeneous absorption profile affects the relative mode position inside the hole. For simplicity, we only consider one of the mode positions, but the principles are the same for both modes.

Without an inhomogeneous absorption profile, the mode spacing is given by the FSR of the cavity. As we do not modify the refractive index in this case, the spacing is simply given by the refractive index of the host material (≈ 1.8) and the physical length of the cavity (21 mm). The modes are spaced a few GHz apart. Inside a TW the group refractive index can be very high, which forces the modes to move in frequency and bunch together, with a typical FSR_{win} on the order of tens of kHz. Moving one FSR outside the TW is equivalent to moving one FSR inside it, but the frequency separation will be different. This FSR ratio is given by n_0/n_{g} and can be used as a first approximation for the position of the mode within the TW. This is an approximation because the shift in frequency is also affected by the susceptibility contribution from the inhomogeneous line itself.

If we have a reference mode located inside a window at a frequency ν_{ref} relative to the center of the hole, then we can move the mode frequency to ν_{m} by burning a new TW with a frequency offset delta of $\Delta\nu_{\mathrm{win}}$ compared to the initial window:

$$\nu_{\mathrm{m}} = \nu_{\mathrm{ref}} - \frac{n_0}{n_{\mathrm{g}}}\Delta\nu_{\mathrm{win}} \tag{5.22}$$

Thus, given a known mode position inside a hole, we can with good accuracy move the mode arbitrarily by burning a new TW at some frequency offset.

In **Paper III** we showed this relation for a wide range of frequencies across the inhomogeneous profile. At the time, we were not able to center the mode completely inside the window. This was later shown in **Paper V**. In Fig. 5.10 I have included some detailed data on how the drift rate behaves in this vicinity. By burning an initial window with a center frequency $\Gamma_{\mathrm{win}} = \Delta\nu_{\mathrm{win}} = 0$ we could locate and lock to this initial mode. New windows were then burnt at incremented $\Delta\nu_{\mathrm{win}}$ positions to move the mode, after erasing the previous structure using the RF coil.

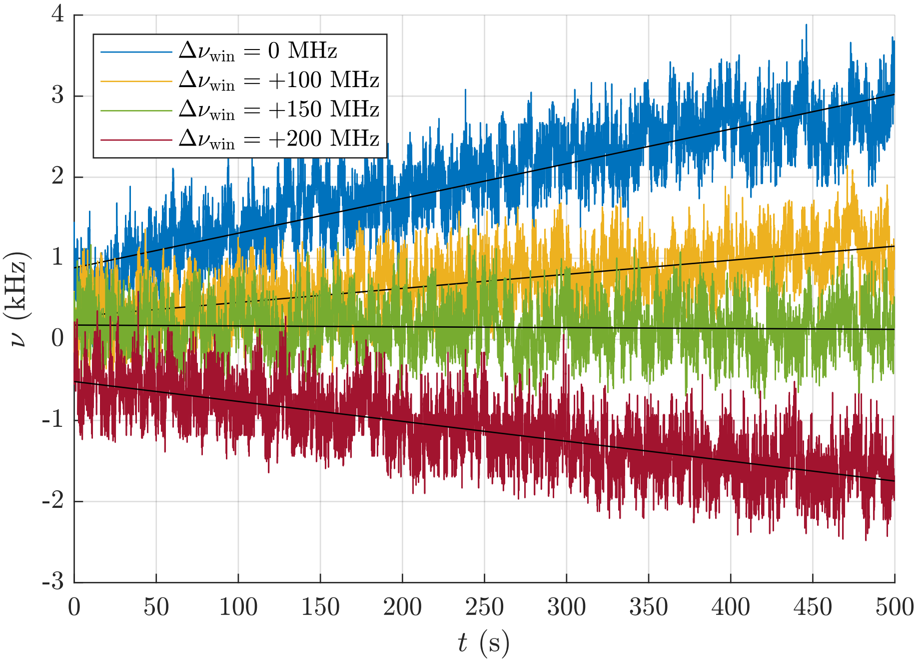

Figure 5.10: Mode drift from single beam locks inside a 50 kHz window. The drift is lower in the center of the hole. Depending on which side of the center the lock is initiated on, the direction (positive/negative) will be different.

We can estimate n_{g} given a TW width Γ_{win} and window edge absorption α_0 from:

$$n_{\mathrm{g}} = \frac{c\alpha_0}{\pi^2\Gamma_{\mathrm{win}}} \tag{5.23}$$

which is approximately 2.5×10^5 for a 50 kHz window with $\alpha_0 = 412\,\mathrm{m}^{-1}$ (using measured peak absorption). The drift data and mode positions have been summarized in Table 5.1. As shown, it is possible to obtain a very low-frequency drift ($0.11\,\mathrm{Hz\,s^{-1}}$) by placing the mode close to the center of the TW.

Table 5.1: Relative mode positions and the corresponding drift around the center point inside a TW. The center frequency of the TW offset to an initial window is given as $\Delta\nu_{\mathrm{win}}$, initial reference mode position as ν_{ref}, ν_{m} is the calculated mode position using Eq. 5.22, and $\nu_{\mathrm{meas.}}$ the measured mode position inside the window. The lowest drift is achieved in the center of the TW.

$\Delta\nu_{\mathrm{win}}$ (MHz)	ν_{ref} (Hz)	ν_{m} (Hz)	$\nu_{\mathrm{meas.}}$ (Hz)	Drift ($\mathrm{Hz\,s^{-1}}$)
0	880	-	-	4.3
100	880	160	280	1.7
150	880	−200	180	−0.11
200	880	−560	−520	−2.5

Returning to dual-beam locking, just as in the case of single-beam locking, the best outcome would be to center both modes. However, as the beams reside on separate spots on the crystal, the absolute length of the cavity can differ. This means that the modes will be located at different positions within the TW. From Fig. 5.4 c) we see the different lengths of the crystal across the face. This will in principle dictate how far the modes are separated in frequency. Based on this, it is advantageous to choose sites on the crystal where the length is similar, given the diameter of your beams. However, to avoid scattering losses, we also need to consider locations with low surface roughness deviations σ_{rms}. For the experiments, a trade-off between the two had to be made. The uncertainty in the placement of the beams on the crystal was approximately 1 mm.

For the dual lock experiment in Fig. 5.9 the modes were separated by $\sim 1\,\mathrm{kHz}$, with initial mode positions $\nu_1 = 2.5\,\mathrm{kHz}$ and $\nu_2 = 3.5\,\mathrm{kHz}$. The modes therefore started to drift apart eventually. Overlapping the modes at this point would have required a frequency shift of about 140 MHz, assuming that the hole hosting the modes had similar shape and properties. This gap could have been closed further by either running the AOM's on negative/positive orders, or by adding in an extra AOM to have a constant shift in one of the arms. The downside of adding in an extra AOM is that this may introduce more noise which cannot be canceled.

During the experiments, we did not manage to close the gap and have the modes centered in the hole at the same time. To move the modes to the center of the TW, a common AOM was used, similar to what was done in Fig. 5.10 for a single-mode lock. The initial positions of the modes were the same as those described above. The frequency was then shifted jointly until one of the modes had low drift. Although the modes were closer to the center, the relative separation between the modes had increased to about 3.4 kHz, making it more difficult to correct. The reason for this may have been due to ion inhomogeneity in the crystal or imperfect burning and/or erasure of transmission windows, which meant that the group refractive index was different for the different modes. The dual beam Allan deviation for these locks were generally lower, between 4 to 6×10^{-14} Hz for τ in the range of 1 to 10 s.

5.3.4 Hole degradation due to locking

After initiating a lock to a mode inside the hole, the hole will start to degrade due to excitation from the locking beam. The degradation can either be symmetric or asymmetric depending on how well the mode aligns with the center. As we have seen in Fig. 5.10, the farther away the mode is from the center of the window, the higher the drift rate. This can be related to asymmetric burning of the window, which removes ions at the edge so that they no longer contribute to the dispersion effect. As this changes the effective length of the cavity, the resonance frequency will shift. In the case of symmetric hole degradation, the ions are excited at an equal rate on either side of the window (Fig. 5.11). Initially, the locking conditions are good, with a narrow mode in the center of the transmission window. As more and more ions are absorbed, the peak absorption will start to decrease and the mode widen. The mode broadening is related to lower dispersion

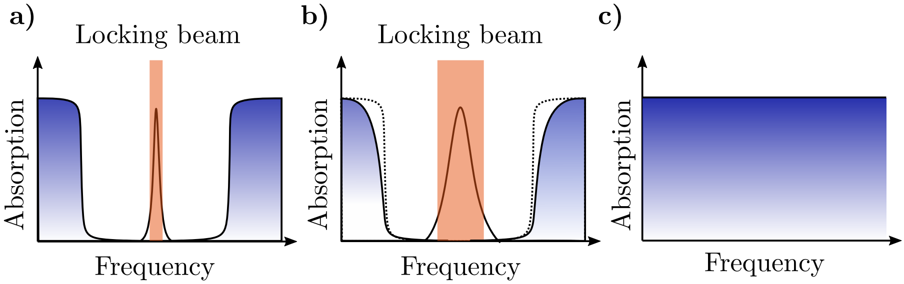

Figure 5.11: Hole degradation due to locking. In a), the initial hole and mode used to initiate the lock. Mode broadening due to hole degradation (b). An equilibrium state is obtained after running RF erasure and resetting the population (c). If the RF fields are applied efficiently, the new window (and cavity mode) will be close to identical to the initial window shown in a).

because of a decreased slow light effect. Thus, the longer the lock, the broader the mode becomes. Eventually, these conditions need to be reset. To re-obtain the initial locking conditions, we can erase the window using RF-pulses. After erasure, the population will return to equilibrium. A new window can then be optically pumped which will share the characteristics of the initial window, resulting in a new narrow mode.

Chapter 6

Summary and outlook

In this work, we have implemented and evaluated a slow-light-based laser frequency stabilization system. Our primary goal was to investigate the extent to which dispersive enhancement of an optical cavity using rare-earth-ion-doped crystals could suppress frequency sensitivity to cavity length fluctuations and how such a system behaves under realistic experimental constraints.

The principal limitation currently appears to be frequency drift, as evidenced by the absence of a well-defined noise floor in the Allan deviation. This suggests that the system's instability is dominated by long-term drift, potentially arising from asymmetric off-resonant excitation. Such excitation can distort the spectral transmission window over time, particularly when the cavity modes are not optimally centered within the window.

To address this, a natural progression is to introduce tighter control over mode positioning within the transparency window. This could be accomplished either by using an additional AOM in the locking loop, enabling independent frequency tuning of both modes, or by designing the system to operate the modes at well-separated frequencies within the inhomogeneous profile. Ideally, both modes should be shifted to the center of the transmission window to minimize differential and absolute drift.

After resolving the drift related issues, further gains in stability could be realized by using a single fiber-coupled electro-optic modulator (EOM) shared between both locking loops. This would make the fiber noise common mode and could therefore be suppressed.

It is important to note that the slow light locking scheme is compatible with other strategies commonly used to reduce thermal noise (mentioned in Ch. 2). These approaches are complementary to our technique and can be considered in future improvements. In particular, to address the dominant source of thermal noise from the cavity mirrors, we could replace the current coatings with monocrystalline mirror coatings. These coatings have mechanical losses that are about ten times lower than those of the conventional amorphous dielectric stacks used on our crystal. Furthermore, while we already benefit from cryogenic operation operating around 2 K, additional improvements could be achieved by cooling to mK temperatures. Of particular interest here is the recent work by Lin et al.[86] which investigated the temperature dependence of spectral hole frequencies in Eu:YSO crystals below 1 K. A ”magic temperature” point was discovered near 290 mK at which the spectral hole frequency becomes first-order insensitive to temperature fluctuations. Thus, operation at this temperature would also have the added benefit of ultrahigh spectral stability. Lastly, increasing the optical mode size on the mirrors reduces coating thermal noise by spatially averaging over more atoms. However, we aim to operate on a region of the crystal with minimal scattering losses and wedge angle. This requirement can limit the beam size in practice, as larger beams sample more of the surface, increasing the likelihood that different parts of the beam experience local variations.

Achieving absolute frequency stability, after demonstrating that thermal noise can be suppressed using slow light cavities, requires careful control over several environmental factors. These must be minimized through isolation and stabilization. While this is not a simple task, it is essential for reaching a regime where the laser frequency is limited only by the fundamental noise floor imposed by shot noise in the photodetector.[15] This sets the minimum detectable frequency shift in the error signal, without considering the use of squeezed light.

In conclusion, the current implementation demonstrates the feasibility of slow-light-based frequency stabilization and highlights several avenues for further improvement. Incorporating drift compensation, improving mode control, and refining the optical design can further develop the potential of slow light cavities for use in precision metrology.

References

[1] A. J. Turner, *The Time Museum. Vol. I: Time Measuring Instruments, Part 3: Water-clocks, Sand-glasses, Fire-clocks.* Rockford, IL: The Museum, 1984.

[2] J. R. Knowles, "Opening address at the longitude symposium," in *The Quest for Longitude: The Proceedings of the Longitude Symposium*, pp. 11–12, 1996.

[3] L. Essen and J. V. L. Parry, "An atomic standard of frequency and time interval: A caesium resonator," *Nature*, vol. 176, pp. 280–282, 1955.

[4] H. Margolis, "A brief history of timekeeping," *Physics World*, vol. 31, no. 11, pp. 27–30, 2018.

[5] D. G. Matei, T. Legero, S. Häfner, C. Grebing, R. Weyrich, W. Zhang, L. Sonderhouse, J. M. Robinson, J. Ye, F. Riehle, and U. Sterr, "1.5 micrometer Lasers with Sub-10 mHz Linewidth," *Physical Review Letters*, vol. 118, jun 2017.

[6] B. J. Bloom, T. L. Nicholson, J. R. Williams, S. L. Campbell, M. Bishof, X. Zhang, W. Zhang, S. L. Bromley, and J. Ye, "An optical lattice clock with accuracy and stability at the 10-18 level," *Nature*, vol. 506, no. 7486, pp. 71–75, 2014.

[7] K. Beloy, M. I. Bodine, T. Bothwell, S. M. Brewer, S. L. Bromley, J. S. Chen, J. D. Deschênes, S. A. Diddams, R. J. Fasano, T. M. Fortier, Y. S. Hassan, D. B. Hume, D. Kedar, C. J. Kennedy, I. Khader, and et al., "Frequency ratio measurements at 18-digit accuracy using an optical clock network," *Nature*, vol. 591, no. 7851, pp. 564–569, 2021.

[8] N. Dimarcq et al, "Roadmap towards the redefinition of the second," *Metrologia*, vol. 61, no. 1, 2024.

[9] T. Rosenband, D. B. Hume, P. O. Schmidt, C. W. Chou, A. Brusch, L. Lorini, W. H. Oskay, R. E. Drullinger, T. M. Fortier, J. E. Stalnaker, S. A. Diddams, W. C. Swann, N. R. Newbury, W. M. Itano, D. J. Wineland, and et al., "Frequency ratio of Al+ and Hg+ single-ion optical clocks; metrology at the 17th decimal place," *Science (New York, N.Y.)*, vol. 319, no. 5871, pp. 1808–1812, 2008.

[10] C. W. Chou, D. B. Hume, T. Rosenband, and D. J. Wineland, "Optical clocks and relativity," *Science*, vol. 329, no. 5999, pp. 1630–1633, 2010.

[11] R. Abbott et al., "Observation of gravitational waves from a binary black hole merger," *Physical Review Letters*, vol. 116, feb 2016.

[12] B. P. Abbott et al, "LIGO: The laser interferometer gravitational-wave observatory," *Reports on Progress in Physics*, vol. 72, no. 7, 2009.

[13] C. J. Kennedy, E. Oelker, J. M. Robinson, T. Bothwell, D. Kedar, W. R. Milner, G. E. Marti, A. Derevianko, and J. Ye, "Precision Metrology Meets Cosmology: Improved Constraints on Ultralight Dark Matter from Atom-Cavity Frequency Comparisons," *Physical Review Letters*, vol. 125, no. 20, 2020.

[14] R. W. P. Drever, J. L. Hall, F. V. Kowalski, J. Hough, G. M. Ford, A. J. Munley, and H. Ward, "Laser phase and frequency stabilization using an optical resonator," *Applied Physics B*, vol. 31, pp. 97–105, 1983.

[15] E. D. Black, "An introduction to Pound–Drever–Hall laser frequency stabilization," *American Journal of Physics*, vol. 69, no. 1, pp. 79–87, 2001.

[16] K. Numata, A. Kemery, and J. Camp, "Thermal-noise limit in the frequency stabilization of lasers with rigid cavities," *Physical Review Letters*, vol. 93, no. 25, pp. 1–4, 2004.

[17] S. Amairi, T. Legero, T. Kessler, U. Sterr, J. B. Wübbena, O. Mandel, and P. O. Schmidt, "Reducing the effect of thermal noise in optical cavities," *Applied Physics B: Lasers and Optics*, vol. 113, no. 2, pp. 233–242, 2013.

[18] L. Yu, "Internal thermal noise in the LIGO test masses: A direct approach," *Physical Review D - Particles, Fields, Gravitation and Cosmology*, vol. 57, no. 2, pp. 1–4, 1998.

[19] T. Kessler, T. Legero, and U. Sterr, "Thermal noise in optical cavities revisited," *Journal of the Optical Society of America B*, vol. 29, no. 1, p. 178, 2012.

[20] S. Amairi, T. Legero, T. Kessler, U. Sterr, J. B. Wübbena, O. Mandel, and P. O. Schmidt, "Reducing the effect of thermal noise in optical cavities," *Applied Physics B: Lasers and Optics*, vol. 113, no. 2, pp. 233–242, 2013.

[21] J. Yu, S. Häfner, T. Legero, S. Herbers, D. Nicolodi, C. Y. Ma, F. Riehle, U. Sterr, D. Kedar, J. M. Robinson, E. Oelker, and J. Ye, "Excess Noise and Photoinduced Effects in Highly Reflective Crystalline Mirror Coatings," *Physical Review X*, vol. 13, no. 4, p. 41002, 2023.

[22] D. Kedar, J. Yu, E. Oelker, A. Staron, W. R. Milner, J. M. Robinson, T. Legero, F. Riehle, U. Sterr, and J. Ye, "Frequency stability of cryogenic silicon cavities with semiconductor crystalline coatings," *Optica*, vol. 10, no. 4, p. 464, 2023.

[23] C. Y. Ma, J. Yu, T. Legero, S. Herbers, D. Nicolodi, M. Kempkes, F. Riehle, D. Kedar, J. M. Robinson, J. Ye, and U. Sterr, "Ultrastable lasers: investigations of crystalline mirrors and closed cycle cooling at 124 k," *Journal of Physics: Conference Series*, vol. 2889, p. 012055, nov 2024.

[24] J. M. Robinson, E. Oelker, W. R. Milner, W. Zhang, T. Legero, D. G. Matei, F. Riehle, U. Sterr, and J. Ye, "Crystalline optical cavity at 4 K with thermal-noise-limited instability and ultralow drift," *Optica*, vol. 6, p. 240, feb 2019.

[25] E. Wiens, Q.-F. Chen, I. Ernsting, H. Luckmann, U. Rosowski, A. Nevsky, and S. Schiller, "Silicon single-crystal cryogenic optical resonator: erratum," *Optics Letters*, vol. 40, no. 1, p. 68, 2015.

[26] G. B. Haxel, J. B. Hedrick, G. J. Orris, P. H. Stauffer, and J. W. Hendley II, "Rare earth elements: critical resources for high technology," Fact Sheet 087-02, USGS, 2002. USGS Publications Warehouse.

[27] L. Knutson Udd and T. Leek, "Ytterby gruva." `https://web.archive.org/web/20180107000000*/https://www.fortifikationsverket.se/Documents/Ytterby-gruva.pdf`, 2012. PDF, in Swedish. Published by Fortifikationsverket. Archived on 7 January 2018. Retrieved 6 January 2018.

[28] M. G. Brik and C.-G. Ma, *Theoretical Spectroscopy of Transition Metal and Rare Earth Ions: From Free State to Crystal Field.* World Scientific, 2019.

[29] G. H. Dieke, *Spectra and Energy Levels of Rare Earth Ions in Crystals.* New York: Interscience Publishers, 1968.

[30] J. Friedrich, *Methods for Bulk Growth of Inorganic Crystals: Crystal Growth.* Elsevier, 12 2016.

[31] Wikipedia contributors, "Europium — Wikipedia, the free encyclopedia," 2025. [Online; accessed 9-April-2025].

[32] PVA TePla CGS, "Czochralski process (cz)," 2025. [Online; accessed 9-April-2025].

[33] C. J. Foot, *Atomic Physics.* Oxford: Oxford University Press, 2005.

[34] R. C. Hilborn, "Einstein coefficients, cross sections, f values, dipole moments, and all that," *American Journal of Physics*, vol. 50, no. 11, pp. 982–986, 1982.

[35] B. Jacquier and G. Liu, *Spectroscopic properties of RE in Optical Materials*, vol. 83. 2005.

[36] Y. Ma, Z. Q. Zhou, C. Liu, Y. J. Han, T. S. Yang, T. Tu, Y. X. Xiao, P. J. Liang, P. Y. Li, Y. L. Hua, X. Liu, Z. F. Li, J. Hu, X. Li, C. F. Li, and G. C. Guo, "A Raman heterodyne study of the hyperfine interaction of the optically-excited state $^5\mathrm{D}_0$ of Eu^{3+}:$\mathrm{Y_2SiO_5}$," *Journal of Luminescence*, vol. 202, no. January, pp. 32–37, 2018.

[37] J. J. Longdell, A. L. Alexander, and M. J. Sellars, "Characterization of the hyperfine interaction in europium-doped yttrium orthosilicate and europium chloride hexahydrate," *Physical Review B - Condensed Matter and Materials Physics*, vol. 74, no. 19, pp. 1–7, 2006.

[38] R. Yano, M. Mitsunaga, and N. Uesugi, "Ultralong optical dephasing time in Eu^{3+}:$\mathrm{Y_2SiO_5}$," *Optics Letters*, vol. 16, pp. 1884–1886, Dec. 1991.

[39] R. Yano, M. Mitsunaga, and N. Uesugi, "Nonlinear laser spectroscopy of Eu^{3+}:$\mathrm{Y_2SiO_5}$ and its application to time-domain optical memory," *J. Opt. Soc. Am. B*, vol. 9, pp. 992–997, Jun 1992.

[40] F. Könz, Y. Sun, W. Thiel, L. Cone, W. Equall, L. Hutcheson, and M. Macfarlane, “Temperature and concentration dependence of optical dephasing, spectral-hole lifetime, and anisotropic absorption in Eu^{3+}:Y_2SiO_5,” *Physical Review B - Condensed Matter and Materials Physics*, vol. 68, no. 8, pp. 1–9, 2003.

[41] R. W. Equall, Y. Sun, R. L. Cone, and R. M. Macfarlane, “Ultraslow optical dephasing in Eu^{3+}:Y_2SiO_5,” *Phys. Rev. Lett.*, vol. 72, pp. 2179–2182, Apr 1994.

[42] R. Oswald, M. G. Hansen, E. Wiens, A. Y. Nevsky, and S. Schiller, “Characteristics of long-lived persistent spectral holes in Eu^{3+}:Y_2SiO_5 at 1.2 K,” *Physical Review A*, vol. 98, no. 6, pp. 1–8, 2018.

[43] M. S. Silver, R. I. Joseph, and D. I. Hoult, “Selective spin inversion in nuclear magnetic resonance and coherent optics through an exact solution of the bloch-riccati equation,” *Phys. Rev. A*, vol. 31, pp. 2753–2755, Apr 1985.

[44] I. Roos and K. Mölmer, “Quantum computing with an inhomogeneously broadened ensemble of ions: Suppression of errors from detuning variations by specially adapted pulses and coherent population trapping,” *Phys. Rev. A*, vol. 69, p. 22321, feb 2004.

[45] L. Rippe, M. Nilsson, S. Kröll, R. Klieber, and D. Suter, “Experimental demonstration of efficient and selective population transfer and qubit distillation in a rare-earth-metal-ion-doped crystal,” *Phys. Rev. A*, vol. 71, p. 062328, Jun 2005.

[46] L. Rippe, B. Julsgaard, A. Walther, Y. Ying, and S. Kröll, “Experimental quantum-state tomography of a solid-state qubit,” *Phys. Rev. A*, vol. 77, p. 022307, Feb 2008.

[47] M. Tian, T. Chang, K. D. Merkel, and W. R. Babbitt, “Reconfiguration of spectral absorption features using a frequency-chirped laser pulse,” *Applied Optics*, vol. 50, pp. 6548–6554, Dec 2011.

[48] F. Wang, M. Ren, W. Sun, M. Guo, M. J. Sellars, R. L. Ahlefeldt, J. G. Bartholomew, J. Yao, S. Liu, and M. Zhong, “Nuclear Spins in a Solid Exceeding 10-Hour Coherence Times for Ultra-Long-Term Quantum Storage,” *PRX Quantum*, vol. 6, no. 1, p. 1, 2025.

[49] A. Holzäpfel, J. Etesse, K. T. Kaczmarek, A. Tiranov, N. Gisin, and M. Afzelius, “Optical storage for 0.53 s in a solid-state atomic fre-

quency comb memory using dynamical decoupling," *New Journal of Physics*, vol. 22, no. 6, pp. 0–13, 2020.

[50] S. P. Horvath, C. Shi, D. Gustavsson, A. Walther, A. Kinos, S. Kröll, and L. Rippe, "Slow light frequency reference cavities - proof of concept for reducing the frequency sensitivity due to length fluctuations," *New Journal of Physics*, vol. 24, mar 2022.

[51] J. J. Longdell, M. J. Sellars, and N. B. Manson, "Hyperfine interaction in ground and excited states of praseodymium-doped yttrium orthosilicate," *Physical Review B - Condensed Matter and Materials Physics*, vol. 66, no. 3, pp. 1–6, 2002.

[52] D. Gandolfi, M. Niedermayr, M. Kumph, M. Brownnutt, and R. Blatt, "Compact radio-frequency resonator for cryogenic ion traps," *Review of Scientific Instruments*, vol. 83, no. 8, 2012.

[53] V. Ramaswamy, A. S. Edison, and W. W. Brey, "Inductively-coupled frequency tuning and impedance matching in HTS-Based NMR Probes," *IEEE Transactions on Applied Superconductivity*, vol. 27, no. 4, pp. 1–5, 2017.

[54] R. R. Benoit and N. Scott Barker, "Superconducting Tunable Microstrip Gap Resonators Using Low Stress RF MEMS Fabrication Process," *IEEE Journal of the Electron Devices Society*, vol. 5, no. 4, pp. 239–243, 2017.

[55] S. S. Attar, S. Setoodeh, R. R. Mansour, and D. Gupta, "Low-temperature superconducting DC-contact RF MEMS switch for cryogenic reconfigurable RF front-ends," *IEEE Transactions on Microwave Theory and Techniques*, vol. 62, no. 7, pp. 1437–1447, 2014.

[56] S. Kim, D. Shrekenhamer, K. McElroy, A. Strikwerda, and J. Alldredge, "Tunable Superconducting Cavity using Superconducting Quantum Interference Device Metamaterials," *Scientific Reports*, vol. 9, no. 1, pp. 1–9, 2019.

[57] R. M. Dickstein, S. L. Titcomb, and R. L. Anderson, "Carrier concentration model for n-type silicon at low temperatures," *Journal of Applied Physics*, vol. 2441, no. July, pp. 2437–2441, 1996.

[58] M. Schubert, L. Kilzer, T. Dubielzig, M. Schilling, C. Ospelkaus, and B. Hampel, "Active impedance matching of a cryogenic radio frequency resonator for ion traps," *Review of Scientific Instruments*, 2022.

[59] J. Koivuniemi and M. Krusius, "Parametric amplication with a high-Q LC resonator," *Physica B*, vol. 288, pp. 2147–2148, 2000.

[60] P. Bradley, E. Sorenson, D. Lauria, and L.-A. Liew, "Characterizing MEMS Switch Reliability for Cryogenic Applications such as Quantum Computing," *IOP Conference Series: Materials Science and Engineering*, vol. 1302, no. 1, p. 012027, 2024.

[61] M. J. Pan, "Performance of capacitors under DC bias at liquid nitrogen temperature," *Cryogenics*, vol. 45, no. 6, pp. 463–467, 2005.

[62] J. D. Siverns, L. R. Simkins, S. Weidt, and W. K. Hensinger, "On the application of radio frequency voltages to ion traps via helical resonators,"

[63] M. V. Gulyaev, O. S. Pavlova, D. V. Volkov, E. G. Sadykhov, N. V. Anisimov, and Y. A. Pirogov, "Application of copper plates for frequency tuning of surface wired and wireless MRI coils," *Journal of Magnetic Resonance*, vol. 309, dec 2019.

[64] Y. C. Sun, "Rare earth materiais in optical storage and data processing applications," *Springer Series in Materials Science*, vol. 83, pp. 379–429, 2005.

[65] F. Bloch, "Nuclear induction," *Physical Review*, vol. 70, no. 7-8, pp. 460–474, 1946.

[66] R. P. Feynman, F. L. V. Jr., and R. W. Hellwarth, "Geometrical representation of the schrödinger equation for solving maser problems," *Journal of Applied Physics*, vol. 28, no. 1, pp. 49–52, 1957.

[67] A. Arcangeli, M. Lovric, B. Tumino, A. Ferrier, and P. Goldner, "Spectroscopy and coherence lifetime extension of hyperfine transitions in $^{151}\mathrm{Eu}^{3+}$:$\mathrm{Y_2SiO_5}$," *Phys. Rev. B - Condens. Matter Mater. Phys.*, vol. 89, no. 18, pp. 1–6, 2014.

[68] A. L. Alexander, J. J. Longdell, and M. J. Sellars, "Measurement of the ground-state hyperfine coherence time of Eu-151(3+) : Y2SiO5," *J. Opt. Soc. Am. B-Optical Phys.*, vol. 24, no. 9, pp. 2479–2482, 2007.

[69] A. Tannús and M. Garwood, "Adiabatic Pulses," *NMR in Biomedicine*, vol. 10, pp. 423–434, 1997.

[70] T. L. Harris, G. W. Burr, J. A. Hoffnagle, M. Tian, W. R. Babbitt, and C. M. Jefferson, "Chirped excitation of optically-dense inhomogeneously broadened media using Eu^{3+}:Y_2SiO_5," *OSA Trends in Optics and Photonics Series*, vol. 88, no. 4, pp. 1531–1532, 2003.

[71] J. M. Robinson, E. Oelker, W. R. Milner, D. Kedar, W. Zhang, T. Legero, D. G. Matei, S. Häfner, F. Riehle, U. Sterr, and J. Ye, " Thermal noise and mechanical loss of SiO 2 /Ta 2 O 5 optical coatings at cryogenic temperatures ," *Optics Letters*, vol. 46, no. 3, p. 592, 2021.

[72] Q. Li, A. Kinos, A. Thuresson, L. Rippe, and S. Kröll, "Using electric fields for pulse compression and group-velocity control," *Physical Review A*, vol. 95, no. 3, pp. 1–8, 2017.

[73] M. Sabooni, Q. Li, L. Rippe, R. K. Mohan, and S. Kröll, "Spectral engineering of slow light, cavity line narrowing, and pulse compression," *Physical Review Letters*, vol. 111, no. 18, pp. 1–5, 2013.

[74] B. E. A. Saleh and M. C. Teich, *Fundamentals of photonics; 2nd ed.* Wiley series in pure and applied optics, New York, NY: Wiley, 2007.

[75] E. L. Hahn, "Spin echoes," *Phys. Rev.*, vol. 80, pp. 580–594, Nov 1950.

[76] D. Gustavsson, *Laser Frequency Stabilization Using a Slow Light Cavity.* Phd thesis, Lund University, Lund, Sweden, 2024.

[77] N. G. Basov, R. V. Ambartsumyan, V. I. Zuev, P. G. Kryukov, and V. S. Letokhov, "Nonlinear amplification of light pulses," *Soviet Physics JETP*, vol. 23, 1966.

[78] S. Chu and S. Wong, "Linear pulse propagation in an absorbing medium," *Phys. Rev. Lett.*, vol. 48, pp. 738–741, Mar 1982.

[79] G. Diener, "Superluminal group velocities and information transfer," *Physics Letters A*, vol. 223, no. 5, pp. 327–331, 1996.

[80] A. E. Siegman, *Lasers.* Mill Valley, California: University Science Books, 1986.

[81] M. J. Sellars, E. Fraval, and J. J. Longdell, "Investigation of static electric dipole-dipole coupling induced optical inhomogeneous broadening in Eu3+:Y2SiO5," *Journal of Luminescence*, vol. 107, no. 1-4, pp. 150–154, 2004.

[82] D. R. Leibrandt, M. J. Thorpe, M. Notcutt, R. E. Drullinger, T. Rosenband, and J. C. Bergquist, "Spherical reference cavities for frequency stabilization of lasers in non-laboratory environments," *Optics Express*, vol. 19, no. 4, p. 3471, 2011.

[83] D. W. Allan, "Statistics of atomic frequency standards," *Proceedings of the IEEE*, vol. 54, no. 2, pp. 221–230, 1966.

[84] W. Riley and D. Howe, "Handbook of frequency stability analysis," 2008-07-01 00:07:00 2008.

[85] T. L. Nicholson, M. J. Martin, J. R. Williams, B. J. Bloom, M. Bishof, M. D. Swallows, S. L. Campbell, and J. Ye, "Comparison of two independent sr optical clocks with $1{\times}10$ -17 stability at 103s," *Physical Review Letters*, vol. 109, no. 23, 2012.

[86] X. Lin, M. T. Hartman, B. Pointard, R. Le Targat, P. Goldner, S. Seidelin, B. Fang, and Y. Le Coq, "Anomalous Subkelvin Thermal Frequency Shifts of Ultranarrow Linewidth Solid State Emitters," *Physical Review Letters*, vol. 133, no. 18, p. 183803, 2024.

Scientific publications

Author contributions

Paper i: Highly tuneable cryogenic radio-frequency magnetic field transmitter coil using resonant in-situ switch bank tuning

I carried out the electrical design and simulations of the resonance circuit and the transmitter coil. Experiments were performed on both the initial and final designs, with data collection, analysis, and interpretation also undertaken by me. The manuscript was written by me with valuable input and feedback from the other authors.

Paper ii: Resetting long-lived ground states in Eu:YSO using a highly tunable radio-frequency transmitter coil circuit

I did the main experimental design and planning of the experiments. Data acquisition and data analysis were performed mainly by me. I did the simulations and numerical calculations for the RF pulses. I wrote the manuscript with input and discussions from the other authors.

Paper iii: Using slow light to enable laser frequency stabilization to a short, high-Q cavity

In this article, I assisted in the design and planning of the experiments. I contributed to the development of the experimental setup, including the optical components and the locking loop. I was actively involved in data acquisition alongside the first author and assisted in the analysis and interpretation of the results. I also participated in the refinement of the manuscript by providing input during its preparation.

Paper iv: Pushing the limits of negative group velocity

The experimental work, including the preparations and building of the setup, was in part done by me. I assisted in conducting the experiments and acquiring the data. I provided input for data analysis and the revision of the manuscript.

Paper v: Characterization of intrinsic Brownian noise in slow light cavities via dual-beam interrogation

I contributed to the conceptualization of the study and the design of the experiments. Building of the experimental setup and the collection of data was performed jointly by me and the second author. I made the main contributions for the data analysis. This paper was authored by me, with the support of the other authors through scientific discussion and manuscript refinement.

Printed by Media-Tryck, Lund 2025 NORDIC SWAN ECOLABEL 3041 0903

Faculty of Engineering, LTH
Department of Physics

Lund Reports on Atomic Physics, LRAP 611 (2025)
ISBN 978-91-8104-533-8
ISSN 0281-2762

LUND
UNIVERSITY